

Product Development Team for NEXRAD Enhancements

Quarterly Report – 4th Quarter FY 02

02.6.2 Polarization and Frequency Diversity

Continue development of algorithms that utilize polarization data to detect regions and fields of hydrometeors and non-hydrometeors, particularly those that are hazardous to aviation operations.

a) Current Efforts

(NSSL):

02.6.2.5. Evaluate quality of the dual-polarization system of the research WSR-88D.

One of the enhancements to the WSR-88D weather radar is a polarimetric capability to improve rainfall estimation and identify precipitation type. Implementation of the proof-of-concept scheme (Fig. 1) has been made on the

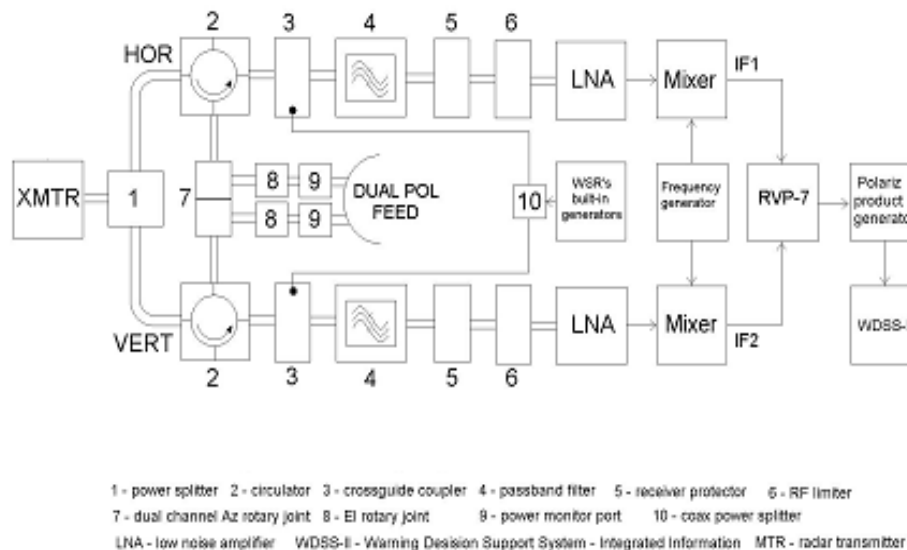


Figure 2.1. Polarization diversity configuration for the NSSL WSR-88D.

NSSL's R&D WSR-88D, and tests are being conducted to determine the quality of this upgrade. The radar transmits and receives horizontally and vertically polarized waves simultaneously. A high voltage power splitter is used to form two channels in the WSR-88D's transmitter, one for the horizontal polarization H and the other for the vertical polarization V. To process vertically polarized

waves, a second receiver, identical to the existing one, has been added (Fig. 1). A commercial (Sigmet RVP-7) processor is passively connected (in parallel with a power PC based processor) to allow sooner test of the engineering quality of the system. This processor requires a sum of offset IF signals, one for the H the other for the V channel. Therefore we have retained the initial 57.54 MHz IF for the H channel and have designed circuits to generate a 63.30 MHz IF for the V channel. The following variables are available on the RVP-7 processor: reflectivity Z_h , Doppler velocity V , and spectral width σ_v , all three at horizontal polarization (as is the case on the WSR-88D network), differential reflectivity Z_{DR} , differential phase shift Φ_{DP} , and correlation coefficient ρ_{hv} between voltages in horizontal and vertical channels.

Two waveguide switches in the transmit chain can be used to bypass the power splitter so that only H waves can be transmitted if needed. Nonetheless, in this mode both H and V waves are received and processed to obtain the linear depolarization ratio LDR and the co-cross-polar correlation coefficient ρ_{hv} in addition to the three spectral moments and the differential phase. In this configuration, the transmitter and the co-polar channel are essentially identical to the existing NEXRAD "legacy" system; the second channel receives the depolarized waves. More detailed description of the modifications made to the NSSL's R&D WSR-88D radar is in the NSSL's internal report (Doviak et al 2002).

The new system has been tested and evaluated for at least six months of operation since March 2002. Different evaluation criteria have been applied regarding the quality of the polarimetric design and data. Among them are minimal value of LDR and maximal value of measured ρ_{hv} in light precipitation. Melnikov et al. (2002a) reported minimal reliably measured LDR values better than -30 dB in light rain which is an indication of a good isolation between two orthogonal channels. Typical maximal values of the cross-correlation coefficient ρ_{hv} measured in light rain with strong SNR are about 0.995. This ensures high accuracy of the measurements of the two basic polarimetric variables that are used for rainfall estimation and hydrometeor classification: KDP and ZDR (Bringi and Chandrasekar 2001). Another indication of the good quality of the radar system is high stability of critical polarization variables such as ZDR. Regular calibration tests performed during the six months period show that the drift of the system bias of ZDR is within 0.1- 0.2 dB (Melnikov et al 2002b).

02.6.2.6 Begin real time testing of the HCA with the Cimarron polarimetric radar and provide real-time polarimetric data and products to the Norman WSFO

Preliminary versions of the algorithms for rainfall estimation and hydrometeor classification have been implemented in real time. Fields of raw polarimetric variables as well as rain accumulations and results of automatic classification are displayed using NSSL Warning Decision Support System-Integrated Infor-

mation (WDSS-II) system. At lower elevation radar scans during warm season, discrimination is made between rain of different intensity, hail/rain mixture, "large drop" regions, and non-meteorological echoes including ground clutter/AP and biological scatterers (insects and birds). Results of automatic classification can be viewed on the WDSS-II displays at the NSSL and the Norman WSFO as well as on the web <http://www.nssl.noaa.gov/~hondl/radar/koun.html>.

This type of data is provided to the Norman WSFO on the regular basis. Some examples of classification results and fields of raw polarimetric variables are presented in the previous quarterly report (July 2002). It was found that overall performance of the polarimetric HCA is very good provided that key radar variables, Z and Z_{DR} , are well calibrated. Discriminatory power of the cross-correlation coefficient, which does not require calibration, is excellent.

Real-time testing of the HCA indicates that at least three problems have to be addressed in the near future. One of them is improvement in the quality of discrimination at signal-to-noise ratios lower than 20 dB for which both Z_{DR} and ρ_{HV} become biased by noise and appropriate correction is required. Second, more reliable delineation of the echoes caused by ground and biological scatterers is needed. Another important problem is that at long distances (of the order of 200-300 km) contribution from frozen hydrometeors becomes significant even at lowest elevation tilt of 0.5° during warm season. Thus, the list of hydrometeor classes that are currently identified has to be augmented by adding categories of frozen particles.

02.6.2.7 Conduct Phase 1 of JPOLE data collection and analysis effort in the warm rain season

Weather observations with the KOUN radar are being conducted on the regular basis. Very few events were missed since May 2002. Raw radar data, rainfall estimation products as well as results of automatic hydrometeor classification are archived and used for in-depth analysis. Existing data set is used for data quality assessment and further development of the rainfall estimation and hydrometeor classification algorithms. Figs. 2.2 and 2.3 illustrate typical PPIs and RHIs of the polarimetric data obtained during the Phase 1 of JPOLE data collection. Both of them demonstrate excellent quality of polarimetric data and tremendous potential of the dual-polarization WSR-88D.

Another important conclusion regards viability of the simultaneous transmission scheme that is selected for the WSR-88D polarimetric design. Even cursory analysis shows that there is no degradation of the quality of polarimetric data compared to the best research dual-polarization radars such as CSU-CHILL and NCAR-SPOL that use traditional alternate scheme of transmission and reception.

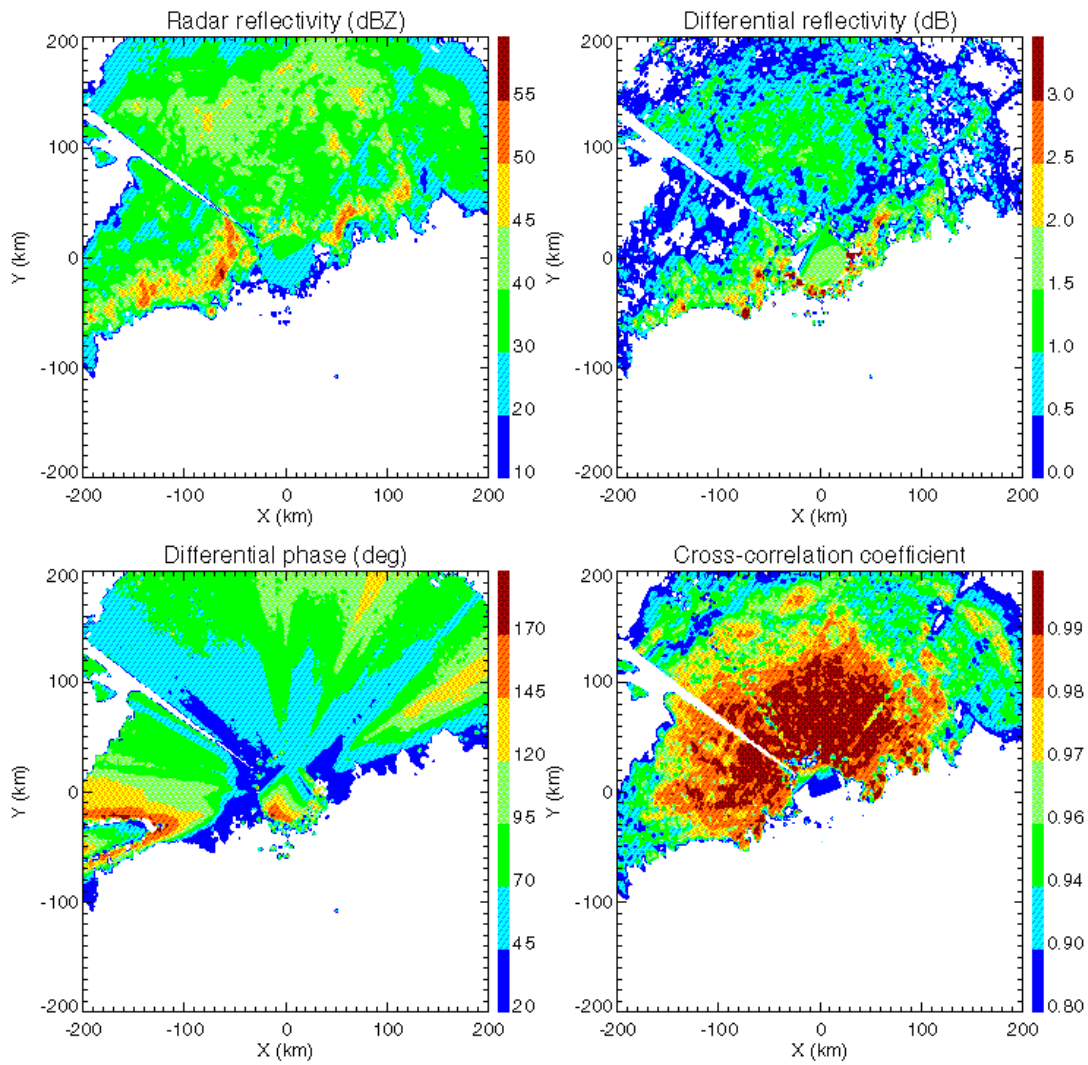


Figure 2.2. Fields of Z , Z_{DR} , Φ_{DP} , and ρ_{hv} at the 0.5° elevation measured by the WSR-88D KOUN radar for the MCS on 16 June 2002, 0201 UTC.

02.6.2.8 Plan Phase 1 of the JPOLE data collection effort for the cold rain/snow season.

Rain/snow discrimination is a big challenge for weather radar observations during cold season. Preliminary analysis of about 30 rain/snow events observed with the NSSL Cimarron radar during last decade indicates that polarimetric contrasts between dry snow and light rain are quite small and superior accuracy of polarimetric measurements is needed to delineate rain and snow. Correct identification of the melting layer or bright band and assimilation of temperature information is probably a key to success. In view of this, our efforts will be directed towards the use of polarimetric information at higher elevations and incorporation of the temperature profiles into the hydrometeor classification

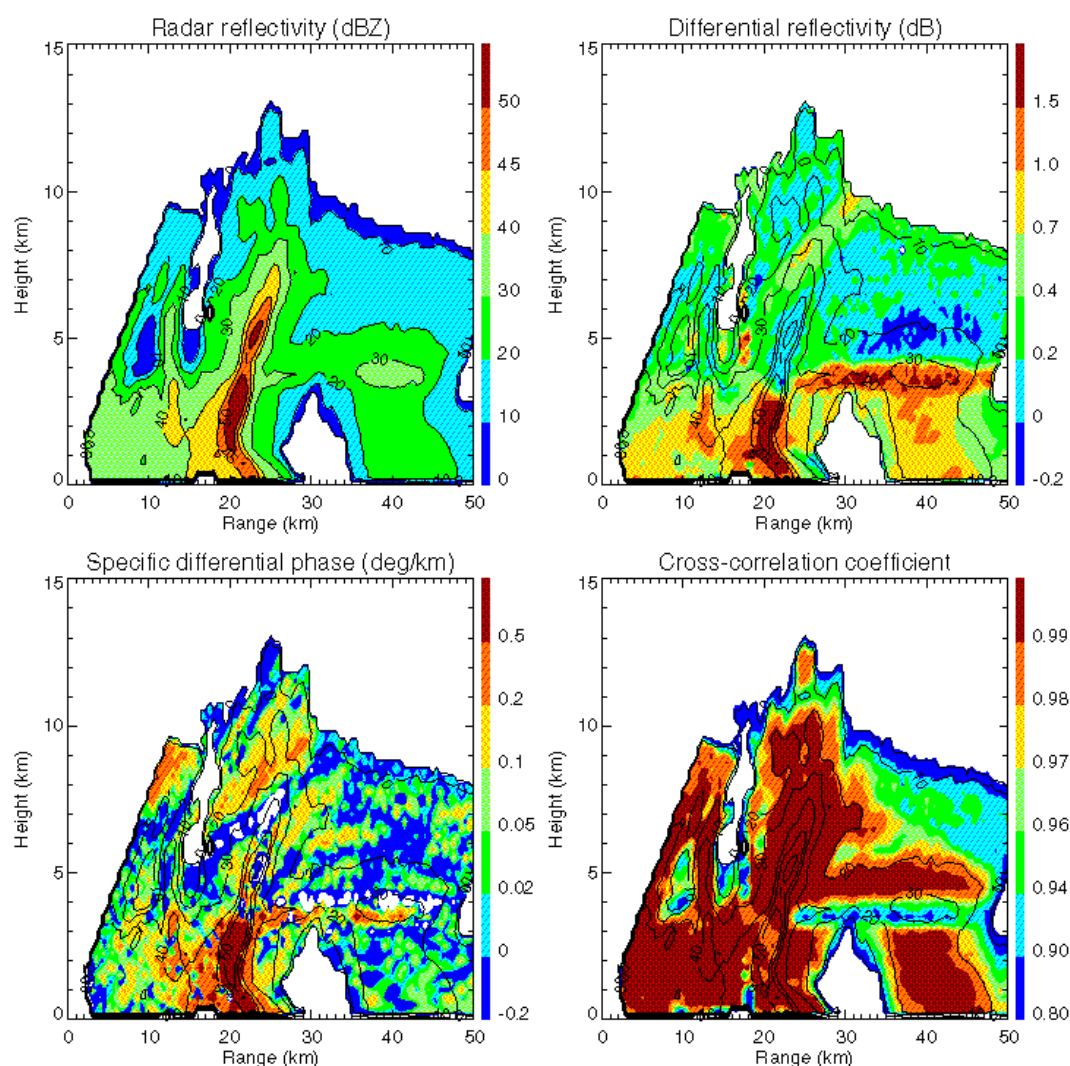


Figure 2.3. Fields of Z , Z_{DR} , K_{DP} and ρ_{hv} measured with the WSR-88D KOUN radar in the vertical cross-section of the storm on 9 June 2002, 0052 UTC.

algorithms. This will imply (a) expanding antenna VCP and making it compatible with existing NEXRAD VCP (currently KOUN collects data only at 0.5 and 1.5° elevation angles) and (b) digesting background temperature information into the HCA. The latter may include temperatures from the Oklahoma Mesonet, soundings, and output of forecast models such as RUC or ARPS.

02.6.2.10 Begin study of a new signal-processing scheme that can decrease volume update times of WSR-88D (or any other weather radar) by a factor of four.

Range oversampling followed by a whitening transformation is a novel method for increasing the number of independent samples from which to estimate the

Doppler spectrum, its moments, as well as several polarimetric variables on pulsed weather radars. The scheme operates on oversampled echoes in range, that is, samples of in-phase and quadrature-phase components are taken at a rate L times larger than the reciprocal of the transmitted pulse length. Each set of L correlated samples is then transformed into a set of L decorrelated samples using a whitening transformation. Powers and correlations are estimated in the usual way along sample time resulting in L values for each of these estimated quantities. The L values are then averaged, and the classical algorithms can now be used to compute the spectral moments and polarimetric variables. Because powers and correlations are derived from a set of decorrelated samples, the variance of estimates decreases significantly.

Since errors of estimates increase with increased antenna rotation speed, the decreased errors associated with whitening permit the antenna to rotate faster while maintaining the current errors of estimates. It follows that storms can be surveyed much faster than is possible with current processing methods. Alternatively, for a given volume scanning time, errors of estimates can be greatly reduced. These are important considerations in WSR-88D operations.

The substantial improvement from this scheme is only achievable at large signal-to-noise ratios (approximately greater than 15 dB, see Fig. 2.4). This is due to the increase in noise introduced by the whitening transformation. The increased noise results in a loss of radar system sensitivity; thus, in using the whitening technique the operational trade-off is estimate accuracy versus radar system sensitivity. Fortunately, in the WSR-88D the signal associated with its prime missions of storm warning and rainfall monitoring is so strong that the increased noise has little impact on the performance of the system.

When established as operationally viable, the whitening technique on range oversampled data will allow substantial estimate variance reduction and/or faster data acquisition rates. This could be advantageously exploited in a combination of faster data temporal acquisition and denser spatial sampling.

02.6.2.14 Refine a new radar hardware calibration technique using the consistency among polarimetric observations.

Radar calibration is essential for producing and maintaining high quality weather data. The problem of accurate measurements of the reflectivity factor Z and differential reflectivity factor ZDR is further exacerbated at lowest elevations whereby a radar beam can experience partial beam blockage.

One of the great advantages of a dual-polarization radar is its capability to measure specific differential phase KDP that is immune to radar system miscalibration and beam blockage. In (Gorgucci et al 1999), the idea of self-consistency among Z , ZDR , and KDP in rain was suggested to assess possible biases in Z provided that both KDP and ZDR are measured accurately. In the presence of

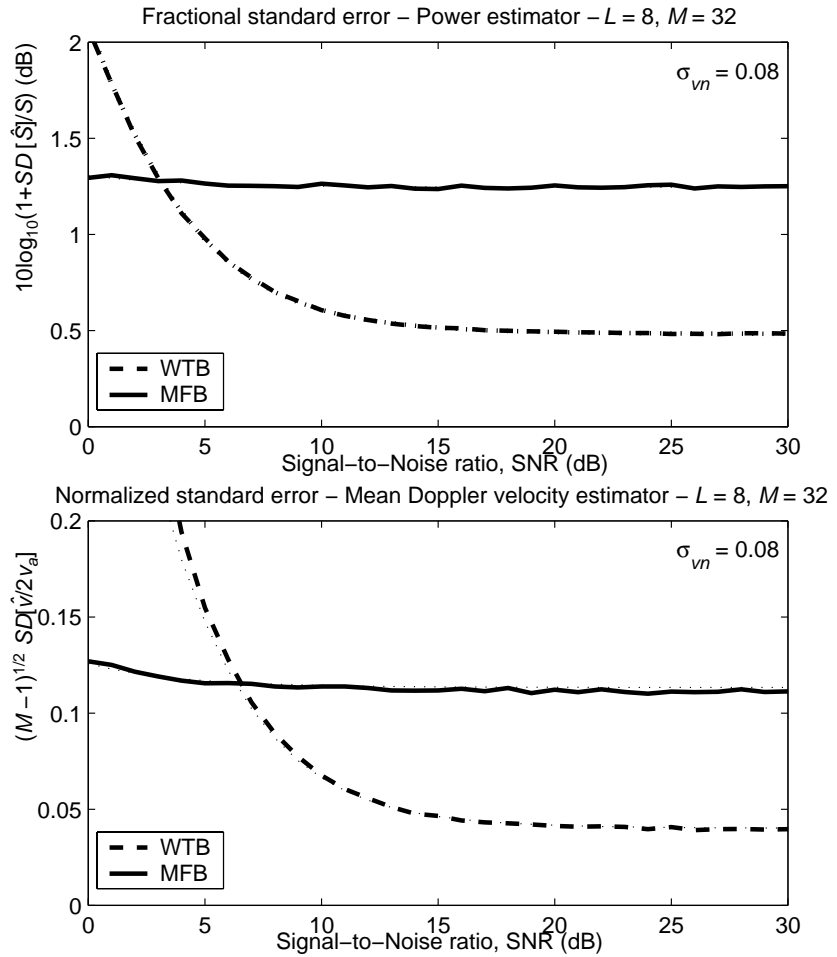


Figure 2.4. Normalized variance of whitening-transformation-based (WTB) and matched-filter-based (MFB) estimators of power (top) and mean Doppler velocity (bottom) versus the signal-to-noise ratio (SNR) for an oversampling factor $L = 8$, 32 pulses, and a normalized spectrum width ($\sigma_{vn} = \sigma_v/2v_a$) of 0.08.

beam blockage, both Z and ZDR are biased and this precludes direct application of the proposed scheme.

A new calibration technique was developed at NSSL (Ryzhkov et al 2002) that is based on the idea of self-consistency and allows to correct Z and ZDR if both of these variables are corrupted due to system miscalibration and radar beam blockage. Some of the results concerning application of this technique towards Z_{DR} calibration are presented in the April 2002 NEPDT quarterly report. Since then we have made assessment of the performance of the suggested scheme for calibration of radar reflectivity.

In order to do this assessment, we compare the performance of the Cimarron polarimetric radar and conventional WSR-88D KTLX radar regarding rainfall estimation over a dense network of rain gages in central Oklahoma. This network numbers 42 gages. Eight rain events were examined for this purpose. It

was found that the Cimarron radar reflectivities measured at the elevation of 0.5° were usually 5 - 12 dB (depending on the case) lower than the ones measured by the KTLX. This points to severe blockage of the Cimarron radar beam in the azimuthal sector containing gage network as well as serious system miscalibration. After polarimetric correction for blockage and miscalibration was made, the estimates of the one-hour rain accumulations from the Cimarron and KTLX radar were compared. The standard NEXRAD $R(Z)$ relation was used to convert Z to rain rate R .

Fig. 5 shows that the Cimarron radar yields better estimates of rainfall than

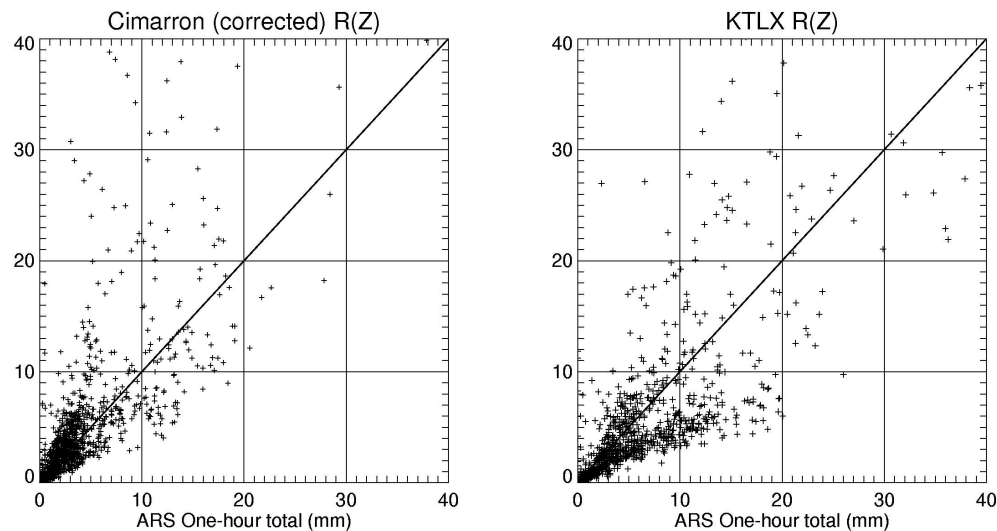


Figure 2.5. One-hour individual gage rain accumulations versus their estimates from the Cimarron radar (with corrected Z) and KTLX radar. Total number of rain events is 8, number of gages is 42, total number of hours of observations is 27.

KTLX after reflectivities measured by the Cimarron radar have been corrected. Moreover, operational WSR-88D radar itself suffers from calibration problems. More detailed analysis shows that for rain events before the year 1999 the KTLX radar tended to underestimate rain, whereas after the year 1999 it mostly overestimated rain as bimodal type of the scattergram in Fig. 5b suggests. This change in the KTLX radar performance might be attributed to modifications of the calibration procedure about that time. This example clearly demonstrates potential utility of the new calibration technique.

References

- Bringi, V. N. and V. Chandrasekar, 2001: *Polarimetric Doppler Weather Radar. Principles and Applications*. Cambridge University Press. 636 pp.
- Doviak, R.J., J. Carter, V.M. Melnikov, D.S. Zrnic, 2002: Modification to the research WSR-88D radar to obtain polarimetric data. NSSL's report, 49 pp.

Gorgucci, E., G. Scarchilli, and V. Chandrasekar, 1999: A procedure to calibrate multiparameter weather radar using properties of the rain medium, *IEEE Trans. Geosci. Remote Sens.* **37**, 269-276

Melnikov, V.M., D.S. Zrnic, R. J. Doviak, J. K. Carter, 2002a: Status of the dual polarization upgrade on the NOAA research and development WSR-88D. *18th Int. Conf. IIPS*. Boston, AMS, 124 - 126.

Melnikov, V.M., D.S. Zrnic, J.K. Carter, A.V. Ryzhkov, R.J. Doviak, 2002b: Evaluation of polarimetric capability on the research WSR-88D. Submitted to *19th Int. Conf. IIPS*, AMS.

(NCAR):

Much of the effort this past quarter was concerned with the preparation of milestone deliverables.

02.6.2.11: Freezing Level Algorithm

Testing of NCAR's Freezing Level Algorithm on three data sets collected during the IMPROVE II field program in the Cascades in Oregon were completed. Results, summarized in Milestone 02.6.2.E12 "Freezing Level Detection: Interim Report" attached below, suggest that algorithm freezing level designations should be within 0.1 km.

02.6.2.12: Verify the components of the Hydrometeor Classification Algorithm

Evaluation of the HCA is continuing. Recent results with the IMPROVE II dataset are presented in the attached Milestone report 02.6.2.E12 entitled "Hydrometeor classification algorithm development: Progress report". The hydrometeor images have only recently been acquired. Hence, the analyses are preliminary in nature. Overall, the algorithm performs as intended, including designations for irregular ice crystals, dry snow, and wet snow.

As in previous field programs, aircraft involved in IMPROVE I and II encountered icing conditions. Polarimetric radar measurements made during these encounters are often suggestive of liquid precipitation in the region where the icing occurred. An example is given in the report. Progress is hampered by sampling differences in time and space and the relatively few well-documented cases. We think that we can supplement the aircraft observations in this study with radiometer measurements and perhaps get a handle on false alarm rates. However, significant progress will probably require dedicated data collections to address the issue. The Joint Polarization Experiment (JPOLE) and the Alliance Icing Research Study II (AIRS II) are candidate field programs for obtaining the necessary observations.

02.6.2.14: Radar hardware calibration

Two reports (appendices), one entitled “Radar reflectivity calibration using the differential phase measurement: Overview” and one entitled “Radar reflectivity calibration using differential propagation phase measurement” were appended to the August monthly report. These reports were submitted in fulfillment of Milestone 02.6.2.E14. The study indicates that the consistency among polarimetric radar measurements should improve hardware calibrations to within 0.5 dB.

b) Planned Efforts

Continue development of HCA and quality control polarimetric techniques and algorithms. Continue collaboration with the Icing PDTs for real -time and short-term forecasting use of polarimetric radar data.

d) Interface with other Organizations

None.

e) Activity Schedule Changes

None.

02.6.3 Circulations

Display the NSSL Mesocyclone Detection Algorithm (MDA) and Tornado Detection Algorithm (TDA) output to Corridor Integrated Weather System users to establish utility for Terminal Convective Weather Forecast (TCWF) and National Convective Weather Forecast (NCWF) aviation users.

a) Current Efforts

NSSL has implemented a local, linear, least-squares method for calculating derivatives of Doppler radial velocity data. This method uses a range-dependent kernel size to estimate the divergent and rotational components of the radial velocity field. This Linear Least Squares Derivative (LLSD) technique is more robust and stable than earlier methods of calculating azimuthal shear and radial convergence, such as those implemented in NSSL's single-radar Mesocyclone Detection Algorithm. The LLSD method allows velocity derivatives from multiple radars to be easily merged and for these important data fields to be viewed in 3-dimensional space, which is not possible with radial velocity data.

The rotational component of the LLSD is tested on simulated Doppler velocity data of mesocyclone-like vortices of varying size and strength, and compared to the peak-to-peak azimuthal shear for the same vortices. Vortices (Fig. 2.1) are generated based on a combined Rankine Vortex model with random 2 ms^{-1} Gaussian noise. The experiment is repeated 1000 times for the each vortex

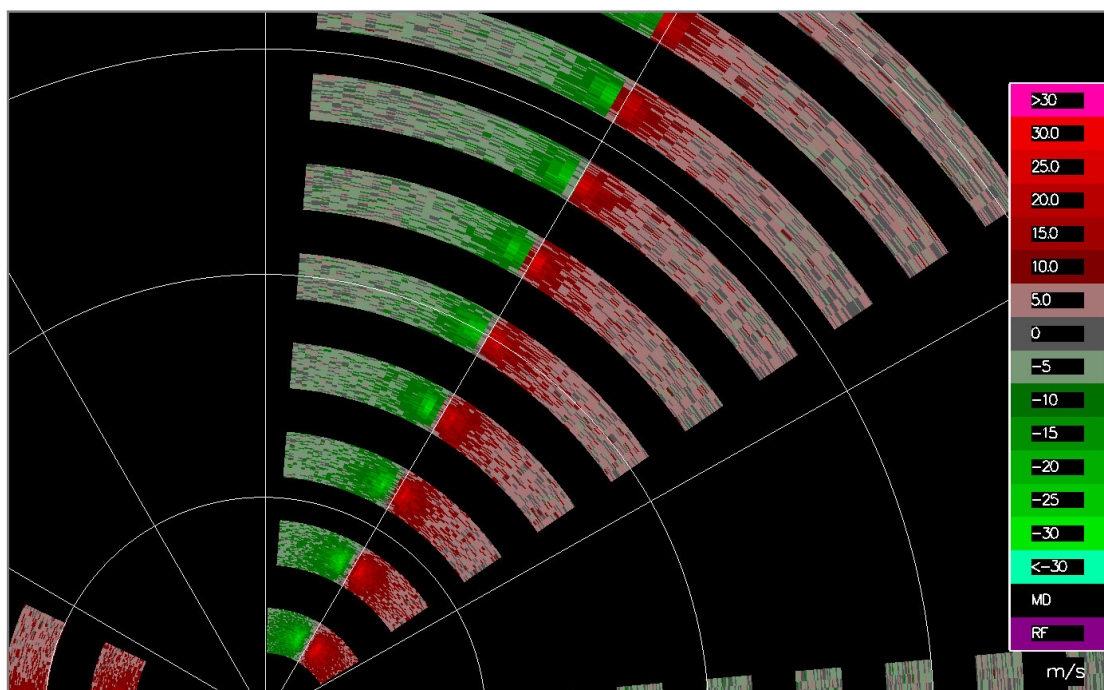


Figure 3.1. Doppler velocity representation of simulated vortices.

size/strength with a different random noise field and random offset of the centerline of the vortex to the middle of the center-most radar beam. This repetition of the experiment allows calculation of confidence intervals for strength and location errors for both the LLSD and peak-to-peak methods of calculating azimuthal shears. The LLSD outperforms the peak-to-peak by having both a more narrow range of maximum shear value estimates and smaller errors in the location of the center of vortices (Figs. 3.2 through 3.6). Additionally, the LLSD estimates of rotation appear as a two-dimensional field of data, whereas traditional peak-to-peak azimuthal are usually given as a single point for each vortex.

Examples of LLSD output from real data are shown in Fig. 3.7 through Fig. 3.9. Fig. 3.7 shows a vertical cross-section of reflectivity data with a bounded weak-echo region, representing a strong updraft along with the corresponding LLSD rotation field, with strong, deep cyclonic rotation (teal) in the updraft location. Fig. 3.8 is a field of maximum LLSD rotation (0.5° and 1.5° elevation angles) over approximately an eight-hour period on May, 3, 1999 (central Oklahoma tornado outbreak), with tornado damage paths overlaid.

This effort lays the groundwork for a multi-radar, multi-sensor, automated vortex detection algorithm. These data may be integrated into multiple-radar mosaics of data fields derived from radial velocity.

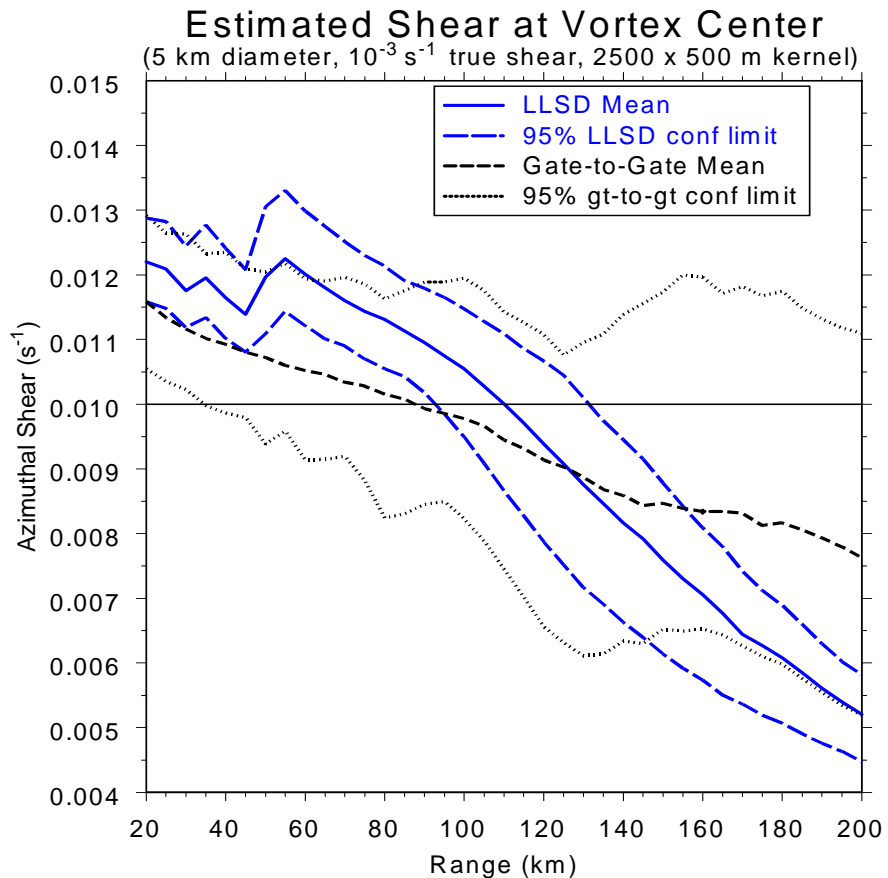


Figure 3.2. LLSD vs. gate-to-gate azimuthal shear estimates and 96% confidence intervals at various ranges.

b) Planned Efforts

Future work includes the development of methods to calculate approximate vortex sizes, which will create greater confidence in the shear strength estimates. Clustering techniques will be applied to these data fields to enable diagnosis of vortices without relying on heuristic rule bases.

c) Problems/Issues

None.

d) Interface with other Organizations

None.

e) Activity Schedule Changes

None.

Positional Error for LLSD 2500x500 m Kernel

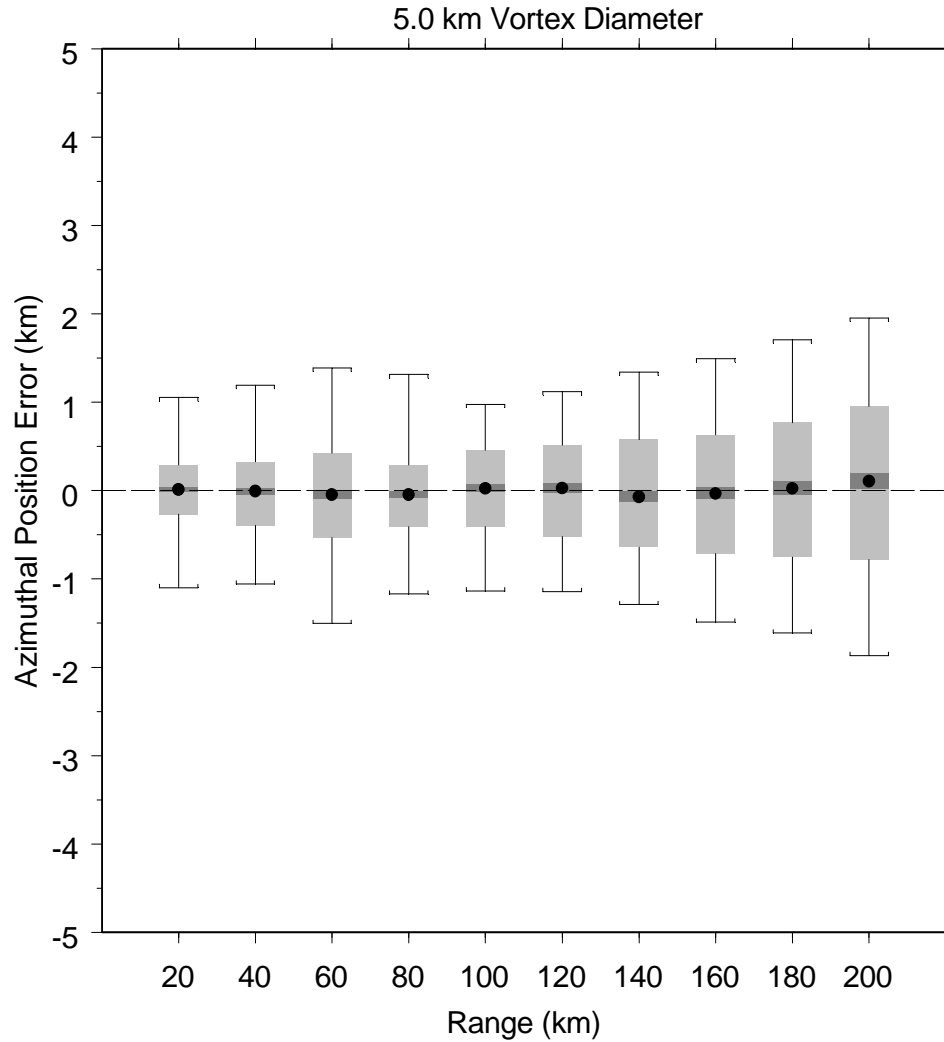


Figure 3.3. Azimuthal positional error statistics for LLSD. Gray bars represent the interquartile range, dark gray bar is the 95% confidence interval for the median, black dot marks the median value and the whiskers extent 1.5 times the interquartile range. Dashed line is zero error.

02.6.4 Technical Facilitation

Continue to develop software infrastructure and tools required for the development and testing and display of NEPDT algorithms.

a) Current Efforts

Software infrastructure and displays were developed for dual polarization radar data and algorithms using output from the Cimarron and KOUN polarimetric radars. In the figures attached, the reflectivity and velocity data from the polarimetric radar are shown, as is the results from polarimetric algorithms (hydrometeor classification, K_{dp} , Φ_{DP} , ρ_{HV} , Z_{dr} and precipitation accumulation).

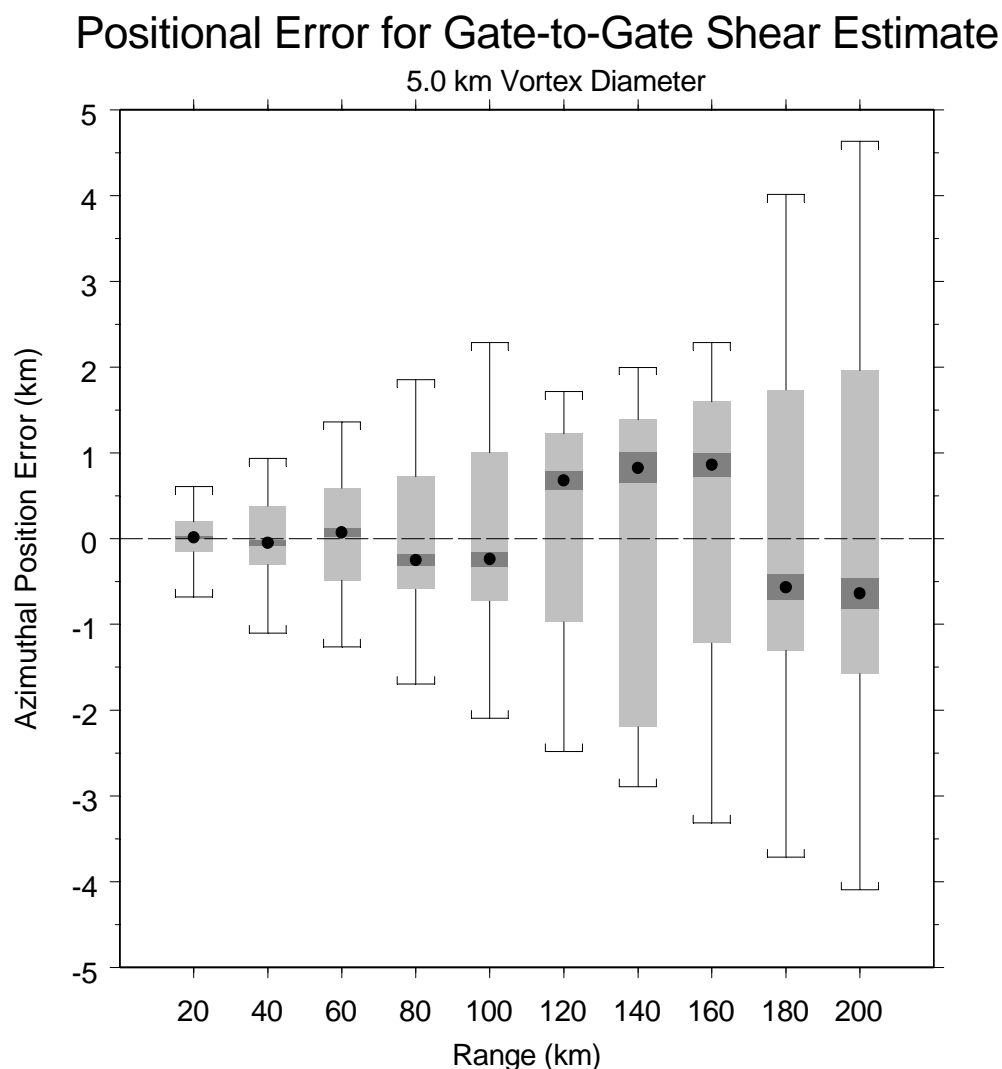


Figure 3.4. Same as Figure 2.3, but for gate-to-gate estimates.

The ingest and algorithms are working real-time. The products are viewable using the WDSS-II display and on the web at <http://www.nssl.noaa.gov/~hondl/radar/index.html>) in real-time. **This meets milestone 02.6.E1 due 30 Sep 2002 to demonstrate this capability.**

Multi-radar composites and composite products have been developed on WDSS-II. In Fig. 4.1 a vertical composite of a merged 3D field from 3 different radars is shown. Since a 3D volumetric field is created, users can fly through the data and create cross-sections (Figs. 4.2 and 4.3). Finally, algorithms such as VIL can be run on the merged 3D field (Fig. 4.4). **This meets milestone 02.6.4.E2 due 30 Sep 2002 to demonstrate this capability.**

Data from multiple sensors can be overlaid and viewed together. Currently, the WDSS-II system can ingest, for algorithm and display use, data from 88D and Terminal Doppler Weather Radar, from polarimetric radar, from GOES satel-

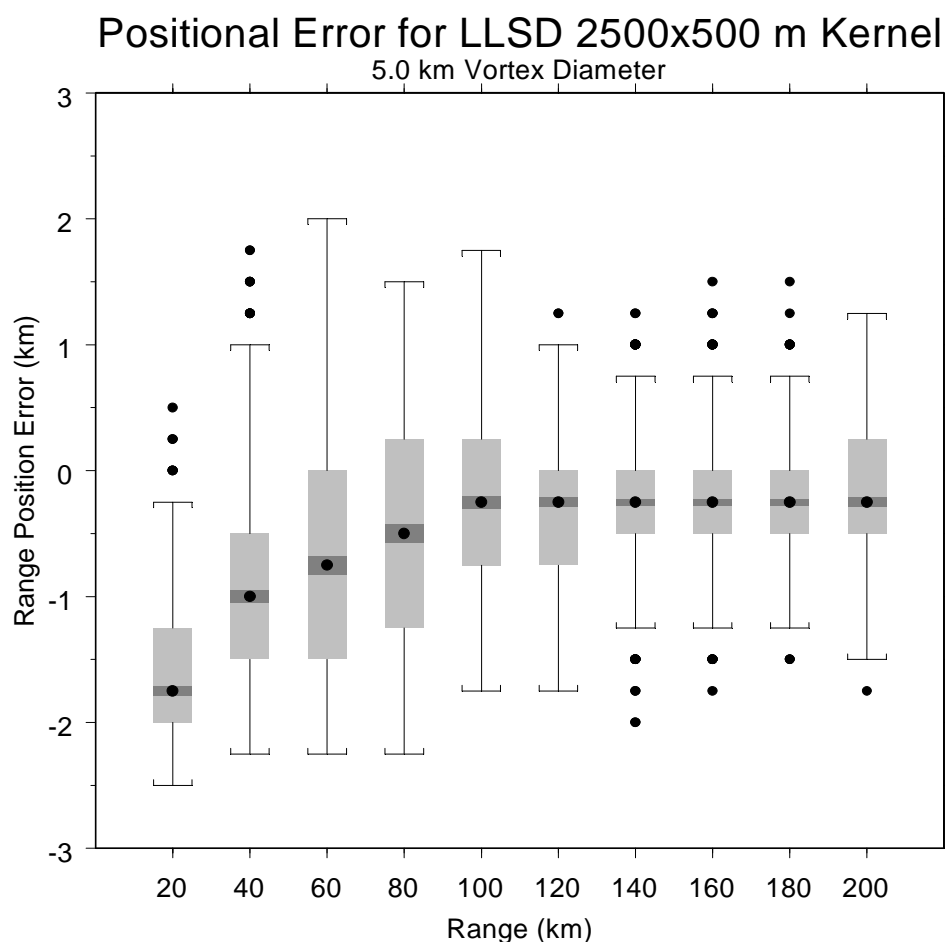


Figure 3.5. Same as Fig. 2.3, but for the LLSD positional errors in range. Black dots mark values outside the interquartile range.

lites, RUC models, mesonet surface observations, NWS warnings and lightning (both 3D mapper and national lightning detection network data). Previous reports have shown imagery from these sources in WDSS-II. **This meets milestone 02.6.4.E3 to develop the infrastructure to demonstrate multi-sensor data display.**

We are also providing support to the following tasks:

- a) Comparisons with new VCPs so that the results of various algorithms can be compared in WDSS-II.
- b) A velocity dealiasing method, based on ancillary work by Qin Xu and others, that works with both 88D and TDWR data using the WDSS-II ingest APIs.
- c) A velocity and reflectivity based wind field retrieval method based on ancillary work by Qin Xu and others that works with both 88D and TDWR data. Initial

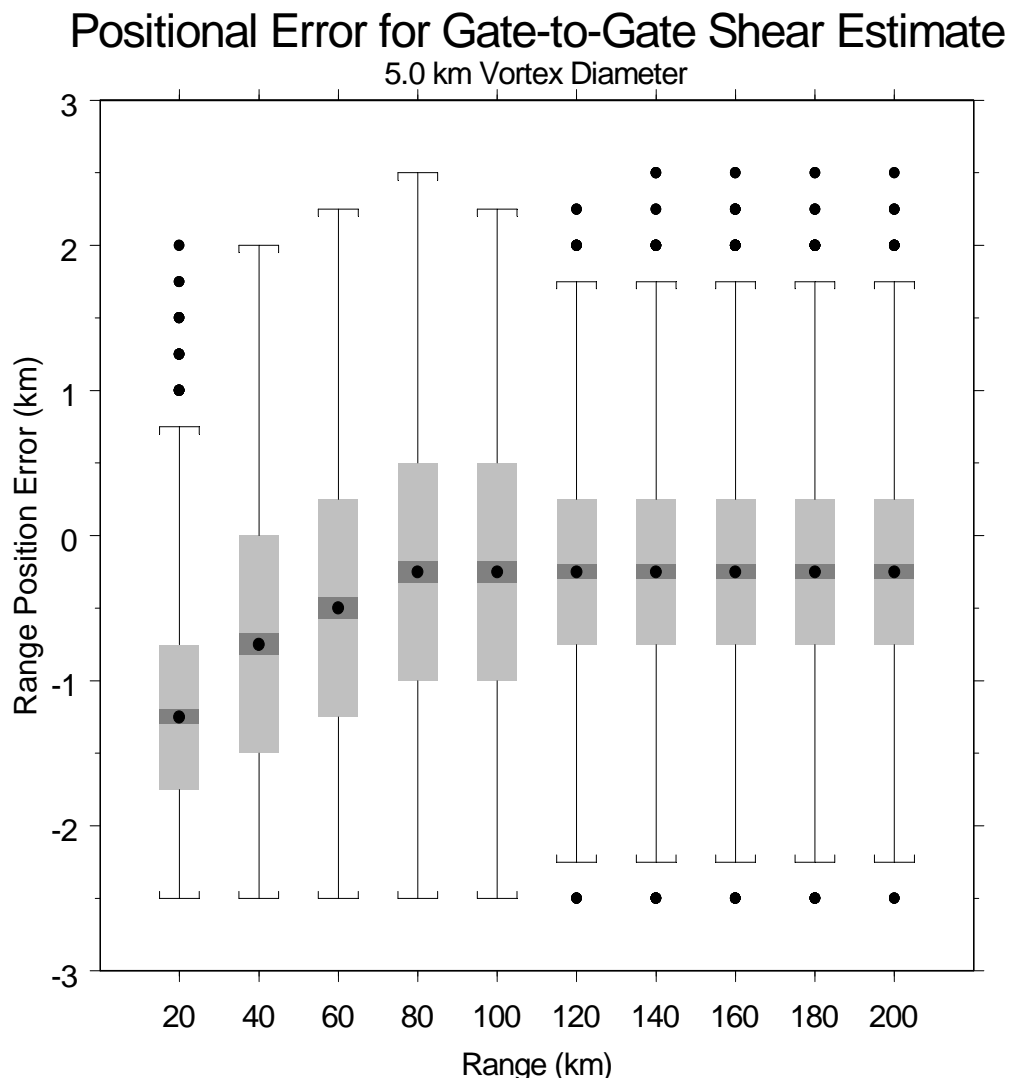


Figure 3.6. Same as for Fig. 2.3, but for gate-to-gate positional errors in range.

examination shows wide variation (up to 50% difference) in the velocity estimates between OKC TDWR and KTLX. We are examining why that is the case.

d) Development of a rotational and divergence product from velocity fields using LLSD. The accumulation of the LLSD field shows remarkable collocation with tornado tracks (Fig. 4.5).

e) The K-Means clustering technique was enhanced to provide motion estimates, and these motion estimates were used to advect individual fields. This work was presented at the AMS Severe Local Storms Conference in San Antonio. The technique now works on 88D, TDWR and satellite fields.

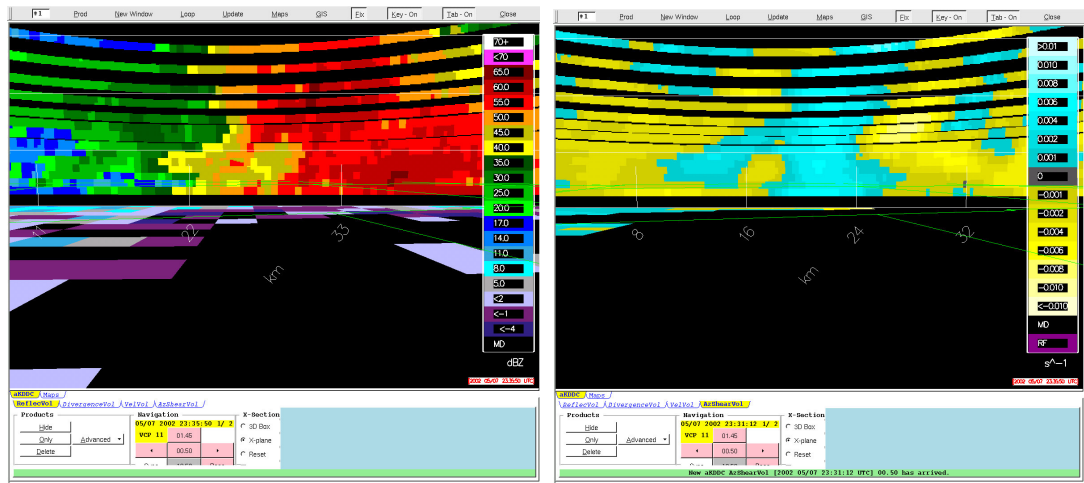


Figure 3.7. Vertical cross-section of reflectivity showing a bounded weak-echo region (right) and rotation corresponding LLSD. Bright teal colors represent strong cyclonic shear of the mesocyclone.

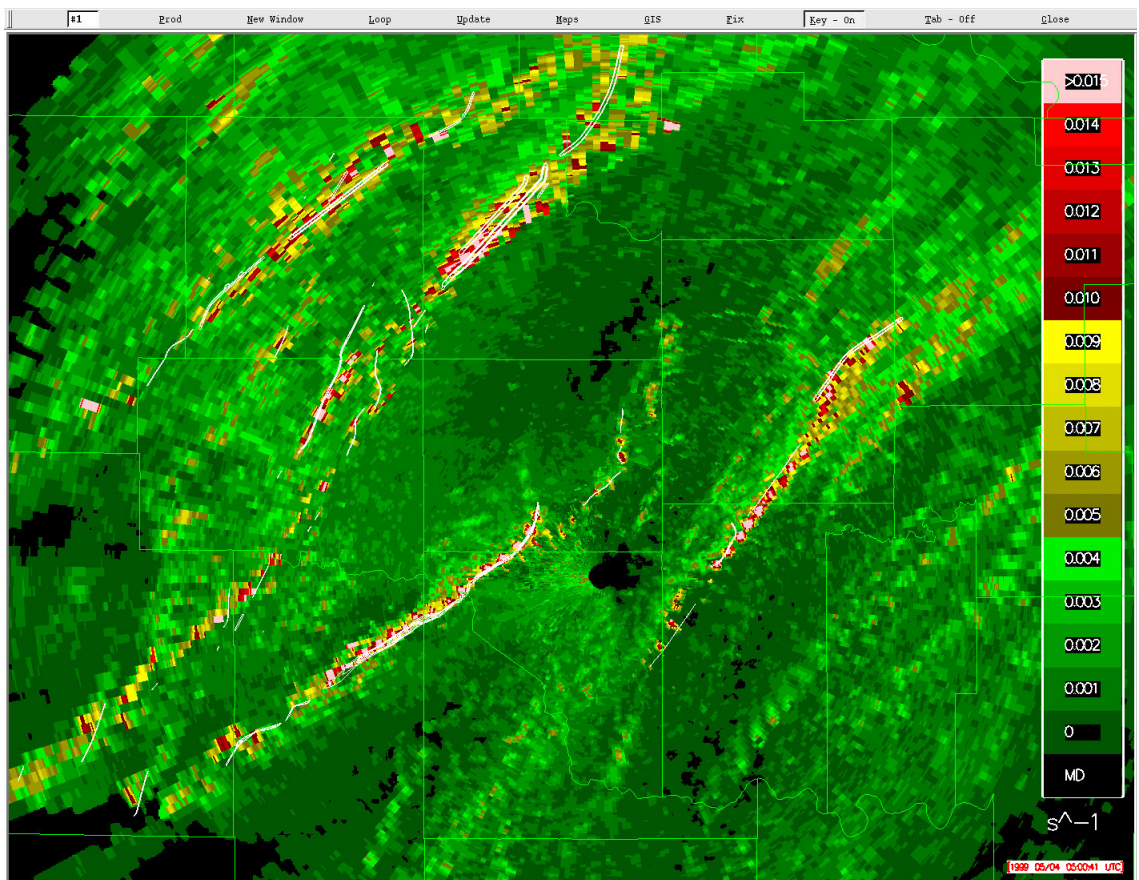


Figure 3.8. Eight-hour LLSD accumulated rotation field for May 3, 1999, showing the tracks of vortex centers. Tornado damage tracks are shown as white contours.

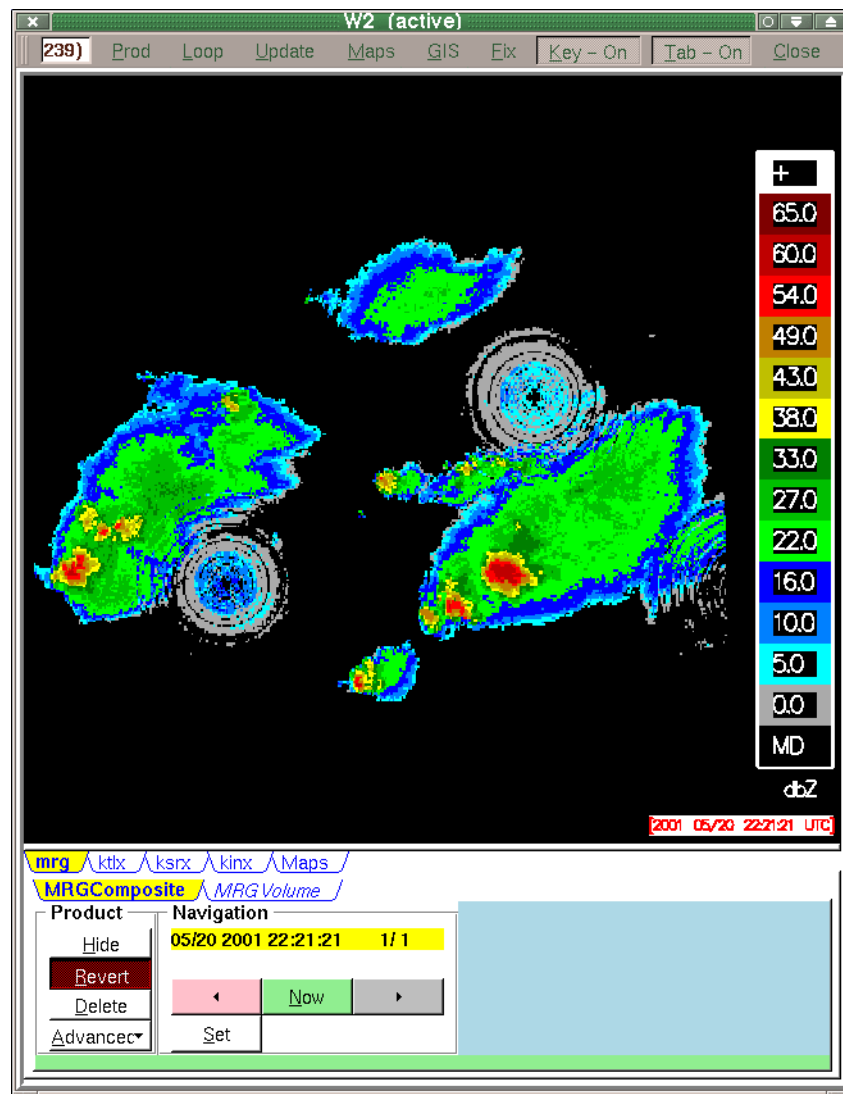


Figure 4.1. Vertical composite of a merged 3D field from 3 different radars.

Figure 4.6 shows the current field and the 15 minute forecast on 88D data. Figure 4.7 shows the current IR temperature field and a 30 minute forecast on satellite infrared data.

f) To enable easy deployment of a suite of algorithms, an easy-to-use controller was developed. Also, to keep up with rapidly changing data sets and to allow user collaboration, work was started on a directory of data sets that the software automatically retrieves for the user.

This directory is retrieved from a web page is shown in Fig. 4.8. The middle part of the figure shows the data sets that various people at NSSL are working on. For example, at the top of the list is a list of radar cases from Aug. 26 (826) and

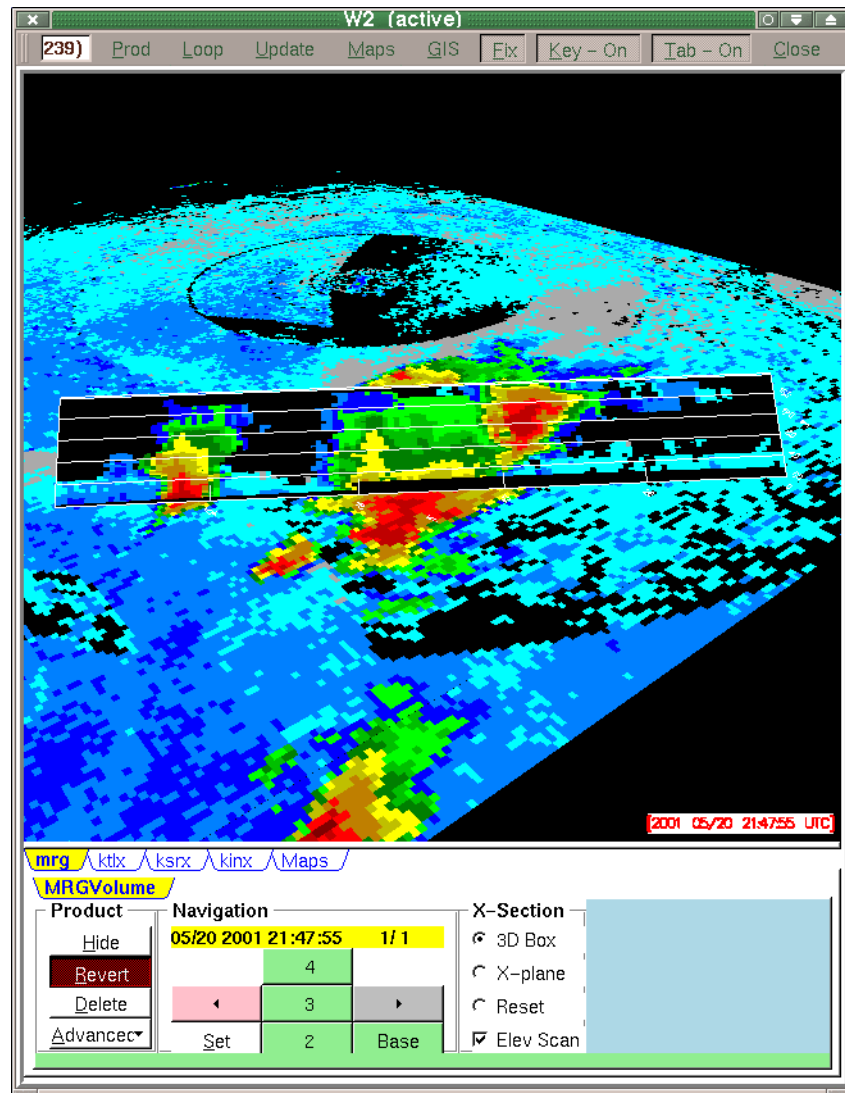


Figure 4.2. “Flythrough” capability for WDSS-II display.

then, further down, a list of real-time high-resolution data feeds including those from satellite, lightning and models.

g) Support for accumulation products, such as hail accumulation. Shown in Fig. 4.9 is a hail accumulation product over-laid with actual tornado tracks.

h) Display enhancements for usability in addition to ingest tasks described above.

b) Planned Efforts

Continue display interface and capability development and enhancement.

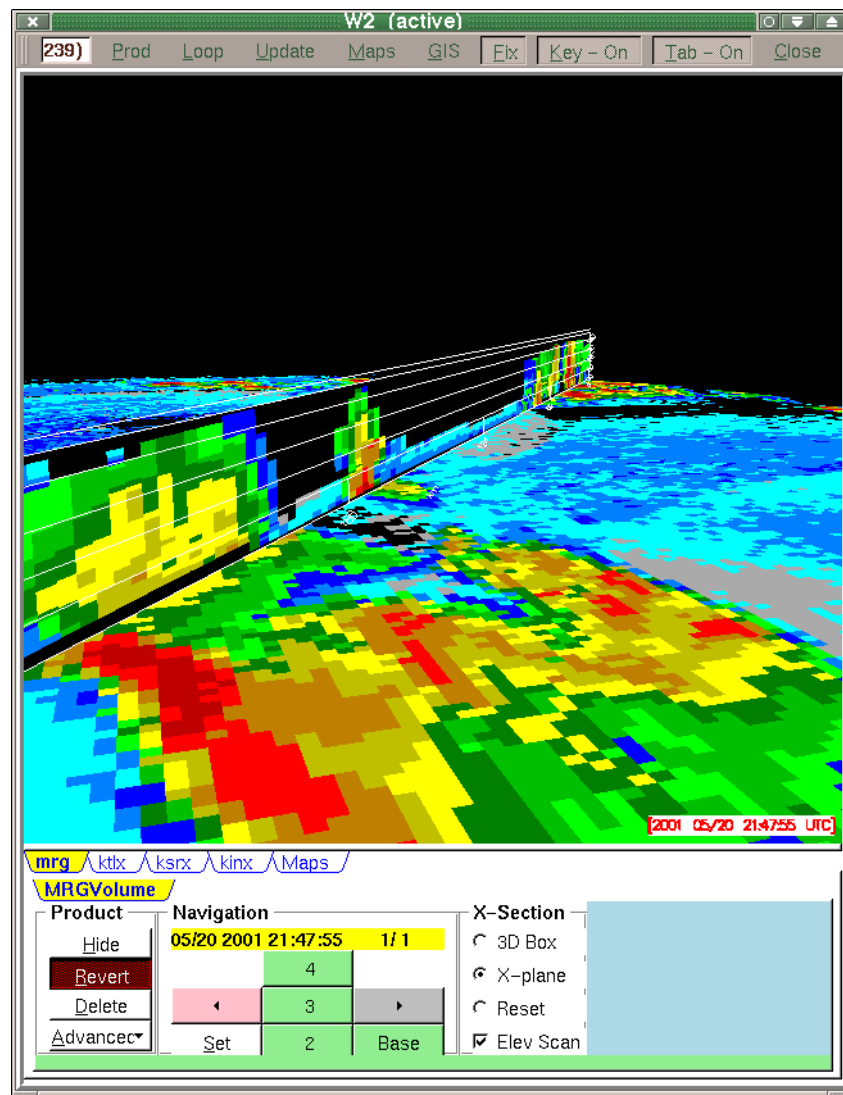


Figure 4.3. Generalized cross-section capability in WDSS-II.

c) Problems/Issues

None.

d) Interface with other Organizations

None.

e) Activity Schedule Changes

None.

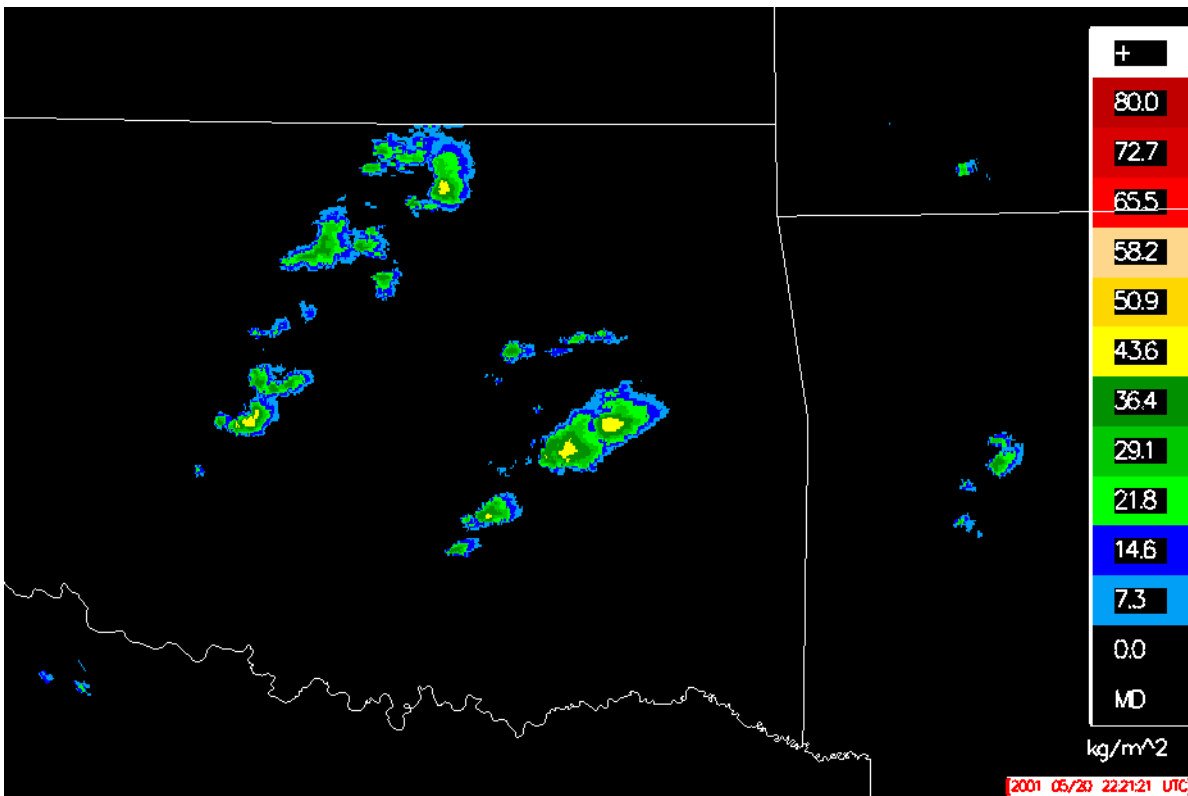


Figure 4.4. VIL display using merged 3D data.

02.6.9 Composite Products

Composite Products - develop a high-resolution multi-radar product with nested resolutions from 500 m to 5 km, that runs in a large analysis domain (such as CIWS), and that is updated at no more than 240 s intervals.

a) Current Efforts

The activities for this quarter include ingesting TDWR data into the real-time 3D mosaic for the CIWS domain and generating bright-band products from both WSR-88D and TDWR data. The system is running for the Oklahoma domain using the Oklahoma City (OKC) airport (Will Rogers) TDWR and 10 nearby WSR-88Ds (KTLX, KFWS, KAMA, KLBB, KFDR, KINX, KVNIX, KICT, KDDC, and KSRX).

To demonstrate the impact of TDWR data, example 3D mosaic products using KINX, KFDR, and OKC are shown in this report. Figures 9.1-9.3 show mosaic reflectivity fields at 1, 1.5, and 2 km above mean sea level (msl) with and without OKC data. It is shown that the TDWR provides additional coverage in the region, especially at the lower levels (Figs. 1 and 2).

Note that TDWR reflectivity has higher resolution (150 m gate spacing) than the current real-time WSR-88D level-2 data (1 km). Figure 9.4 shows that the OKC

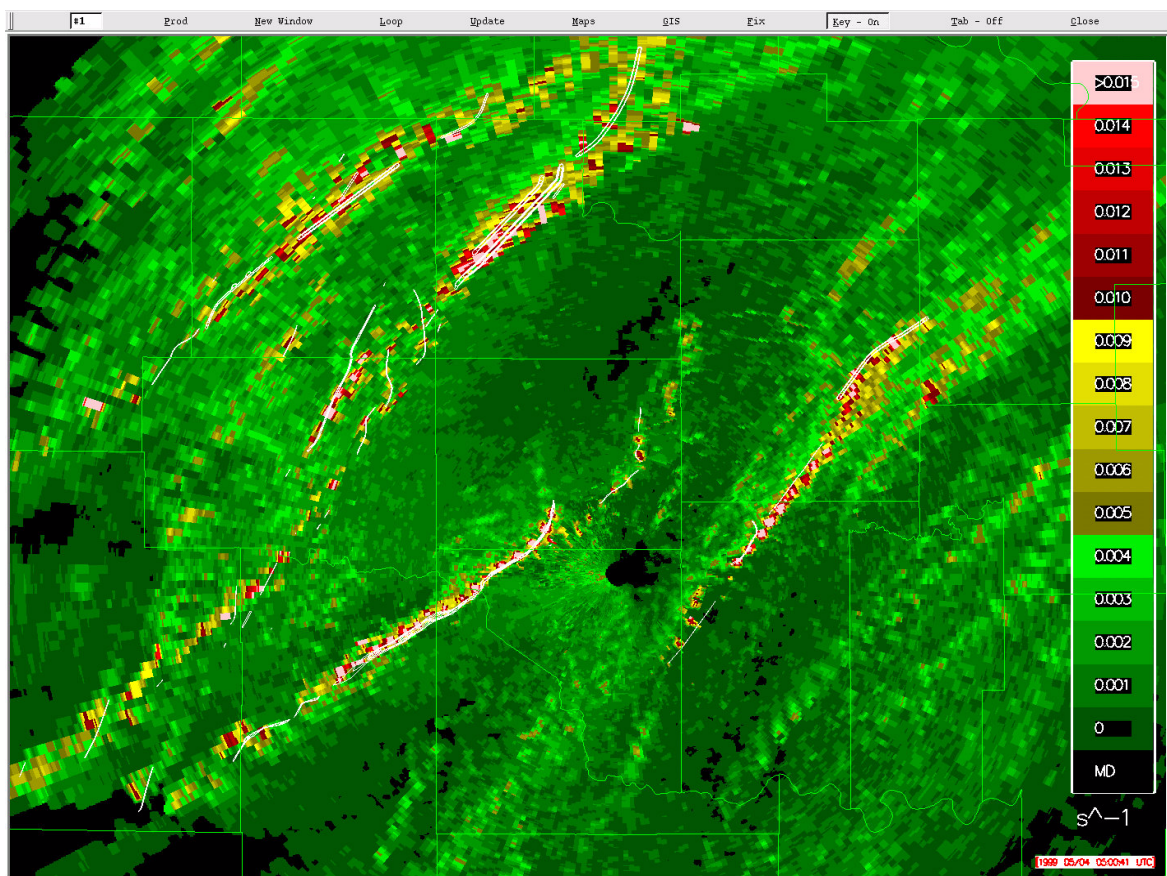


Figure 4.5. Accumulated linear least-squares azimuthal shear tracks.

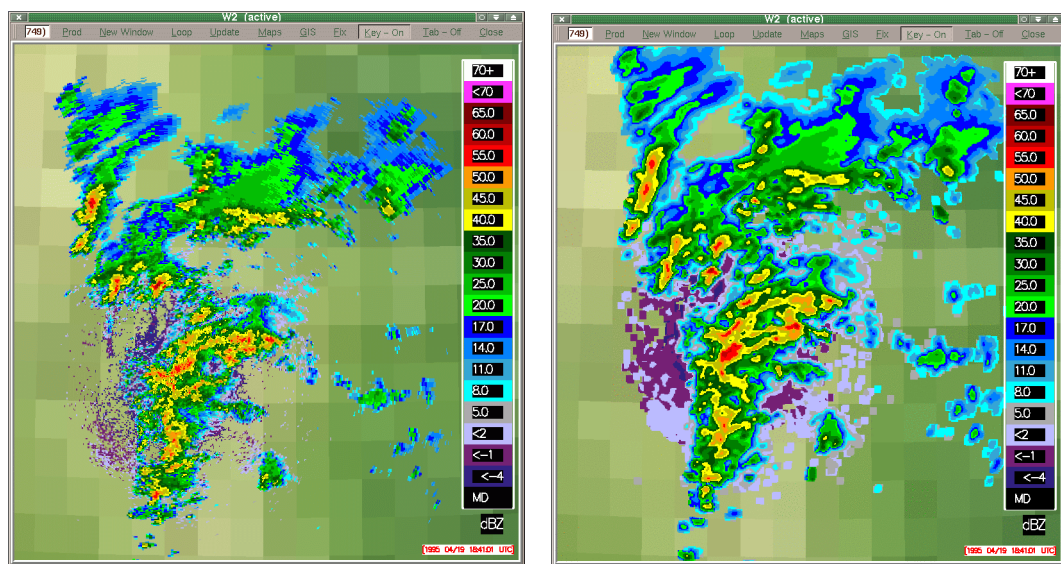


Figure 4.6. Current (left) and 15 min forecast (right) of reflectivity based on K-means cluster techniques.

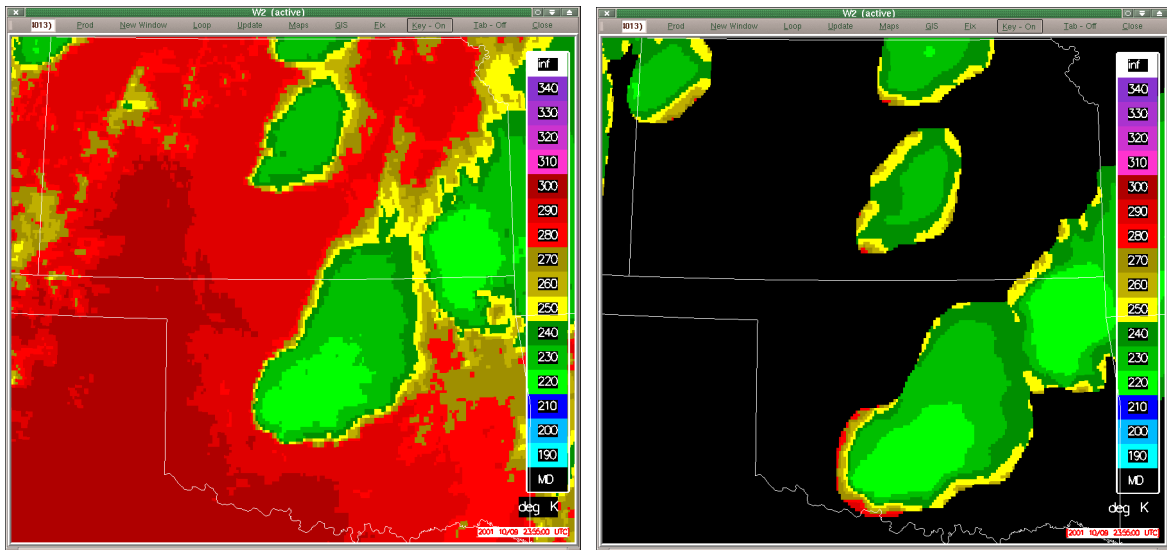


Figure 4.7. Observed satellite IR field (left) and 30 min forecast (right) based on K-means cluster technique.

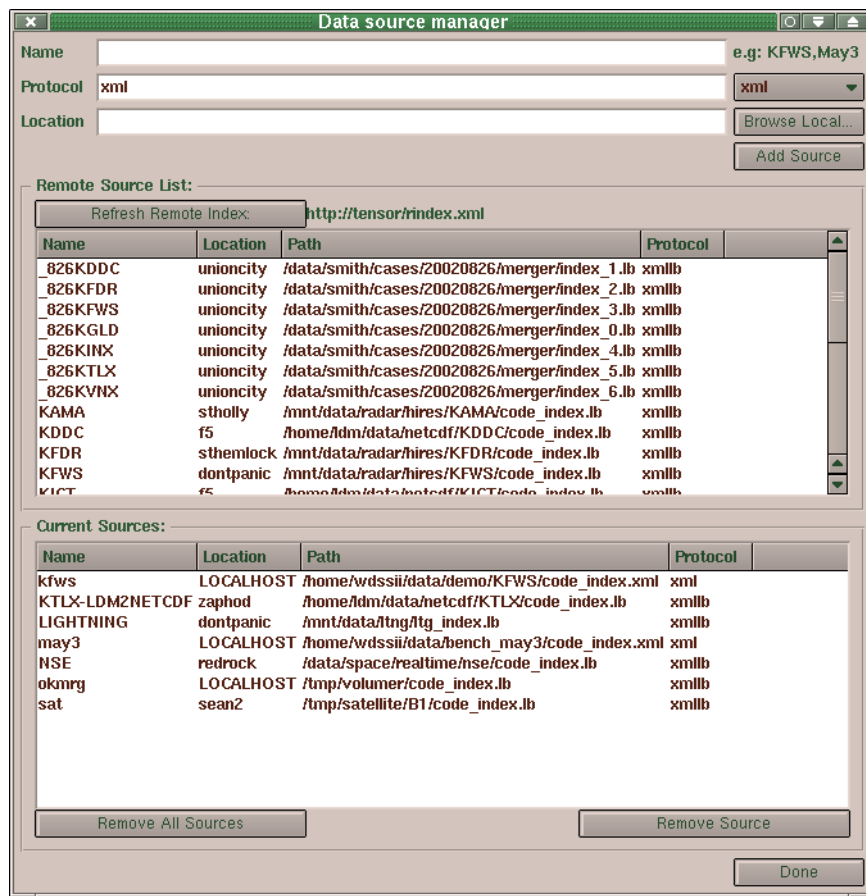


Figure 4.8. Current directory of archived data sets available for WDSS-II application testing.

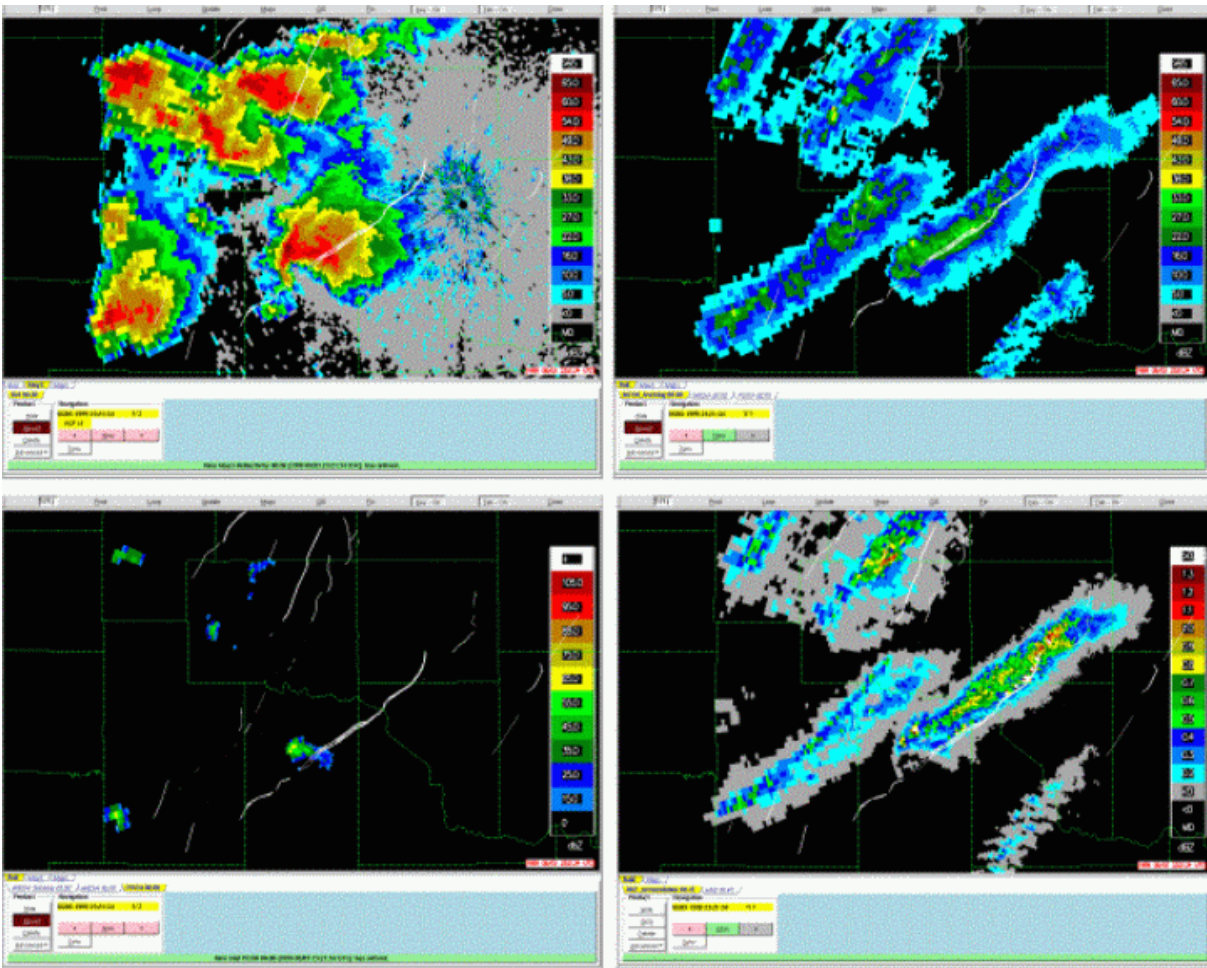


Figure 4.9. Accumulated hail (based on the NSSL hail algorithm) product overlaid with actual tornado tracks.

TDWR reflectivity field contains much finer scale than does the KTLX data. This implies that a higher resolution grid can be used for the 3D mosaic in the vicinity of TDWR region. The finer resolution 3D mosaic can be very useful in diagnosing small-scale phenomena such as microburst.

Due to the fact that this quarter is in convective season for the Oklahoma region, there has been no bright-band detection by any of the radars (WSR-88Ds or TDWR) since the deployment of TDWR BBID (Bright-Band IDentification). The BBID algorithm will run continuously in real-time and results will be reported in the coming quarter(s). Figure 9.5 shows an example bright-band plot from archived case (using KTLX radar). It shows that the bright-band top determined by the BBID algorithm correspond to the RUC analysis very well.

Both deliverables 02.6.9.E1 and 02.6.9.E2 have been met.

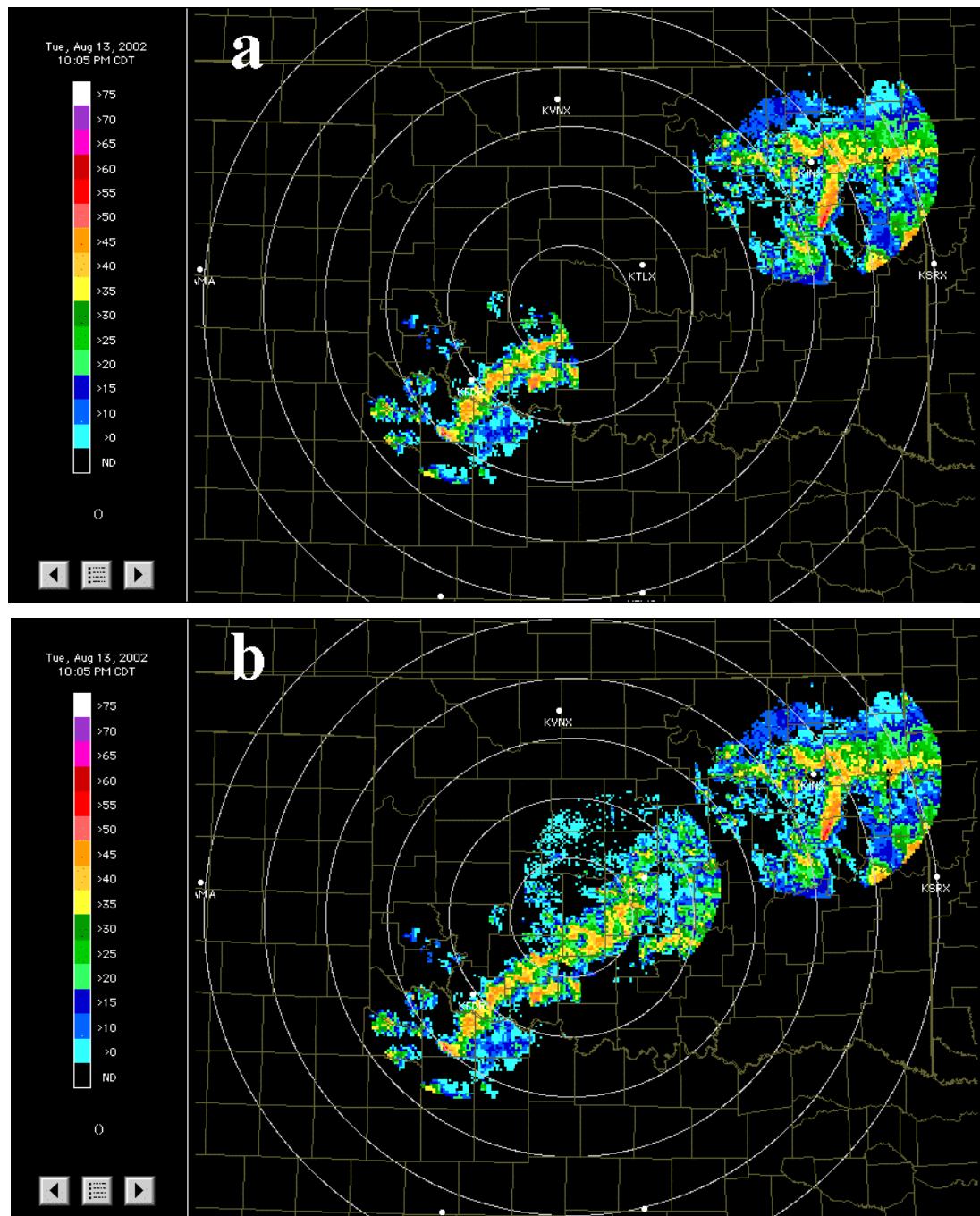


Figure 9.1. Mosaic reflectivity fields at 1km above mean sea level (msl) for a convective precipitation event occurred on 14 August 2002. In panel a, the mosaic field was obtained using data from KINX and KFDR. In panel b, additional data from OKC TDWR radar were used in the mosaic.

b) Planned Efforts

Next quarter we hope to have stratiform precipitation events in the Oklahoma domain so that TDWR BBID results can be collected and reported.

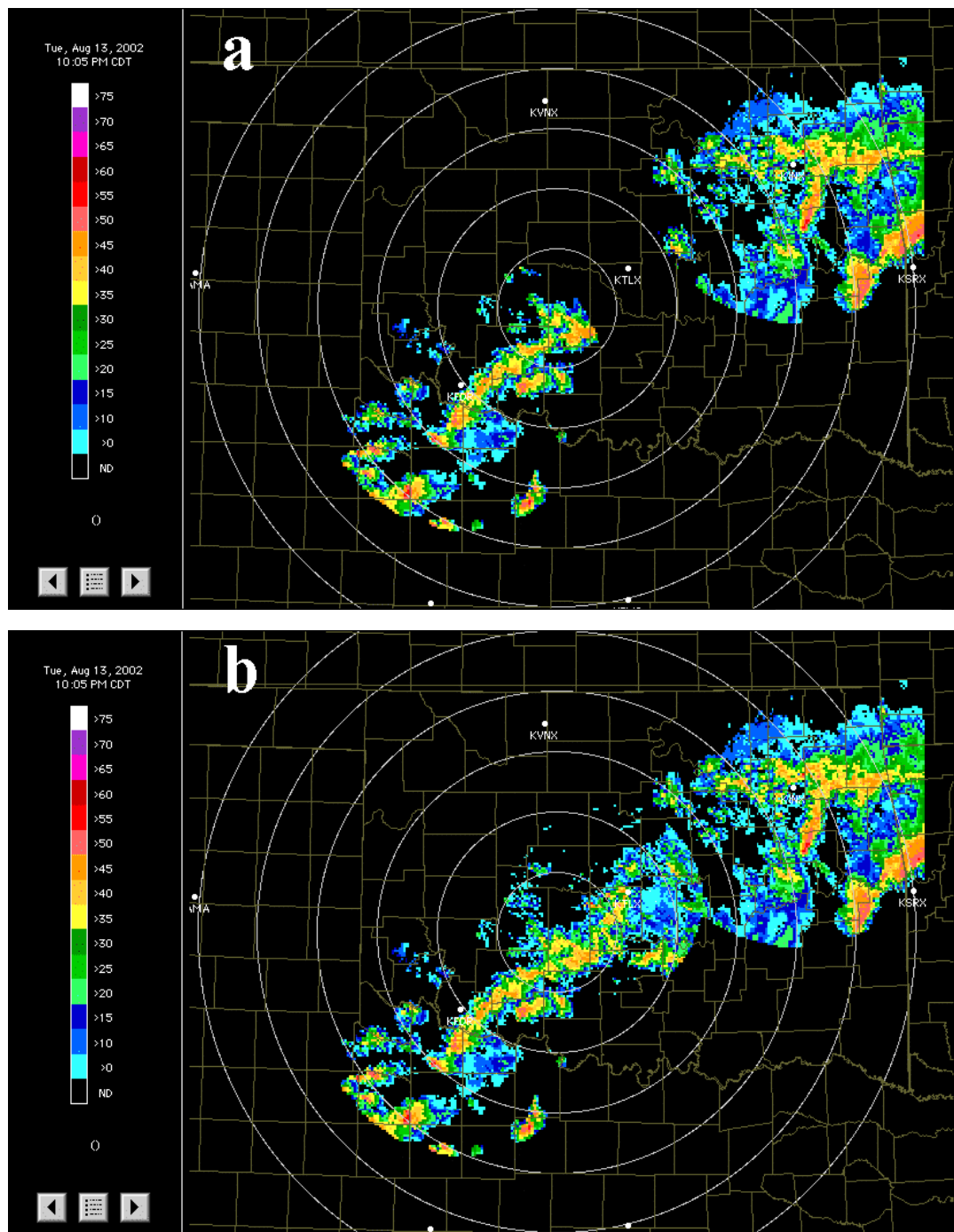


Figure 9.2. Same as in Fig. 9.1 except for at 1.5km above msl.

c) Problems/Issues

None.

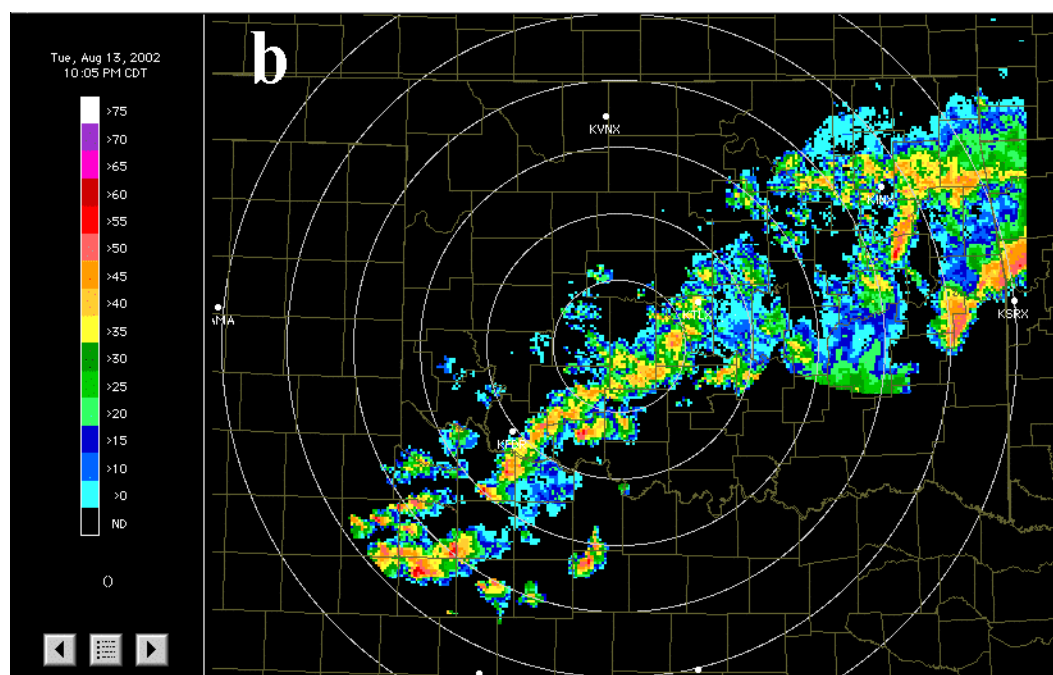
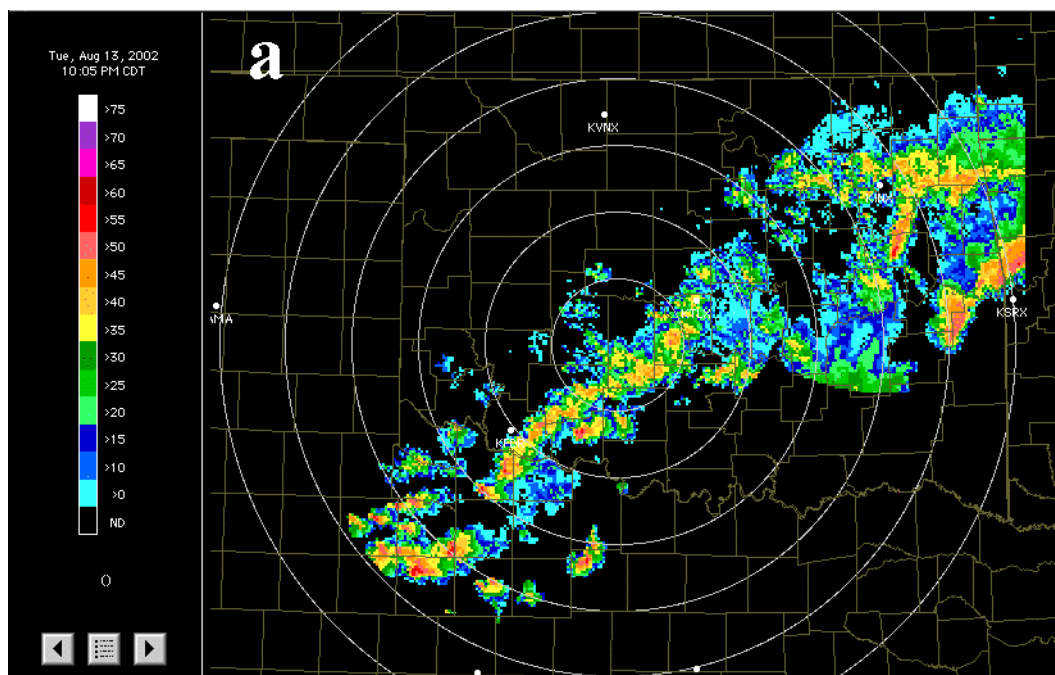


Figure 9.3. Same as in Fig. 9.1 except for at 2km above msl.

d) Interface with other Organizations

None.

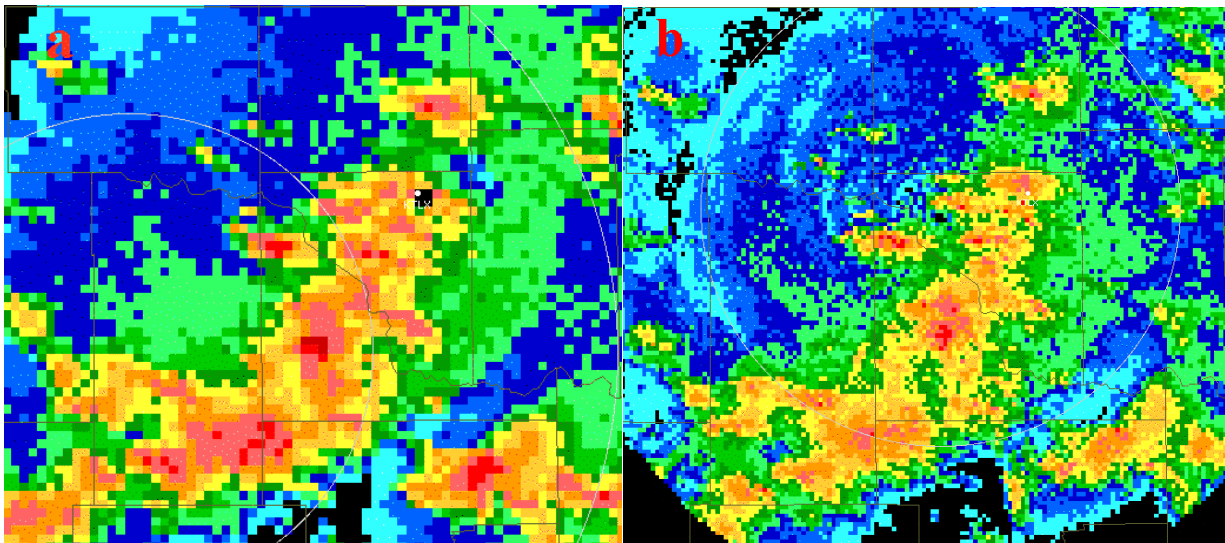


Figure 9.4. Composite reflectivities from KTLX (panel a) and OKC (panel b) radar observations that are valid at 03:05Z on 14 August 2002.

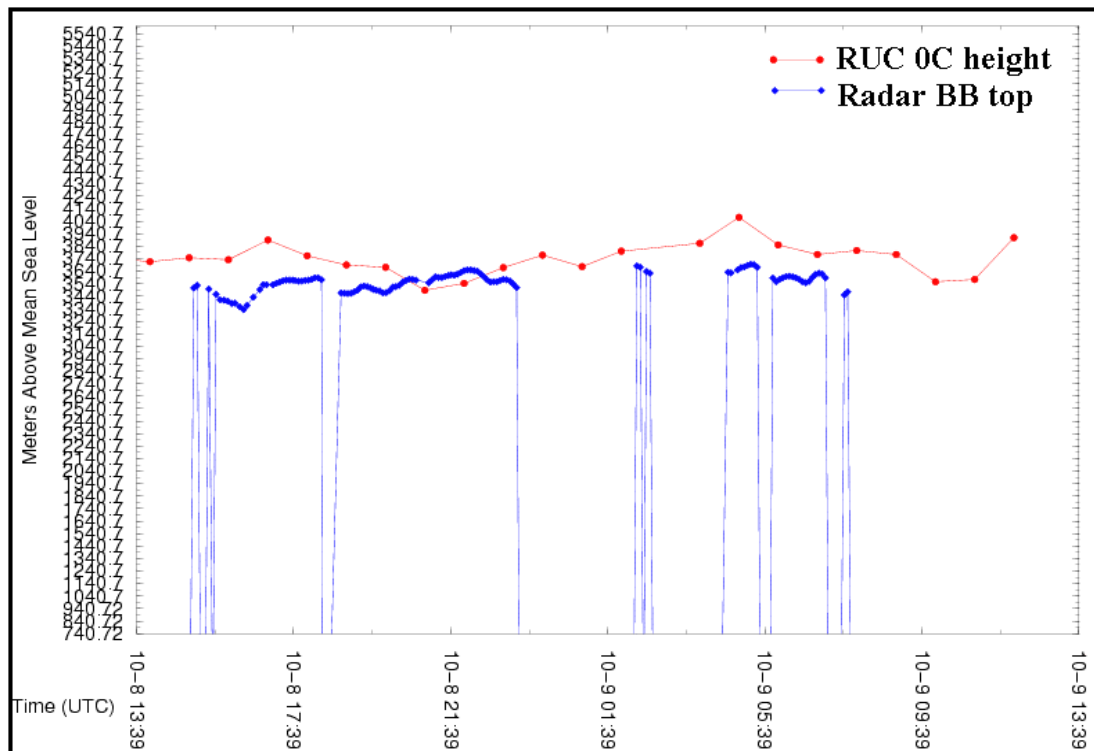


Figure 9.5. Example bright-band plots from KTLX. The abscissa is time and the ordinate is height above mean sea level.

e) Activity Schedule Changes

None.

02.6.11 Volume Coverage Patterns

Volume Coverage Patterns - develop and implement new VCPs to meet the WSR-88D coverage needs of the aviation community and the AWR PDTs.

a) Current Efforts

No results to report.

b) Planned Efforts

Continue collecting data for new VCP patterns as needed.

c) Problems/Issues

None.

d) Interface with other Organizations

None.

e) Activity Schedule Changes

None

02.6.12 Product Implementation

Explore and define aviation-specific products and implementation paths appropriate for NEPDT efforts.

a) Current Efforts

Examination of circulation and associated divergence patterns as they relate to aviation interests. Coordination between MIT/LL, NCAR and NEPDT for distribution of CIWS radar products.

b) Planned Efforts

Continue liaison and development efforts.

c) Problems/Issues

None.

d) Interface with other Organizations

None.

e) Activity Schedule Changes

None

02.6.14 Multi-radar Composites

Examine aspects of multiple radar integration and algorithms.

a) Current Efforts

By the end of last quarter, the 3D multi-radar reflectivity mosaic had been running in real-time for CIWS_A domain (NEPDT 3rd quarter report for year 2002, task 02.6.14). The activities for this quarter include setting up the real-time 3D mosaic for the other two CIWS domains (CIWS_B and CIWS_C) and generating products. By the end of August, all three domains are up and running. Figures 14.1-14.3 show example real-time products from each individual domain.

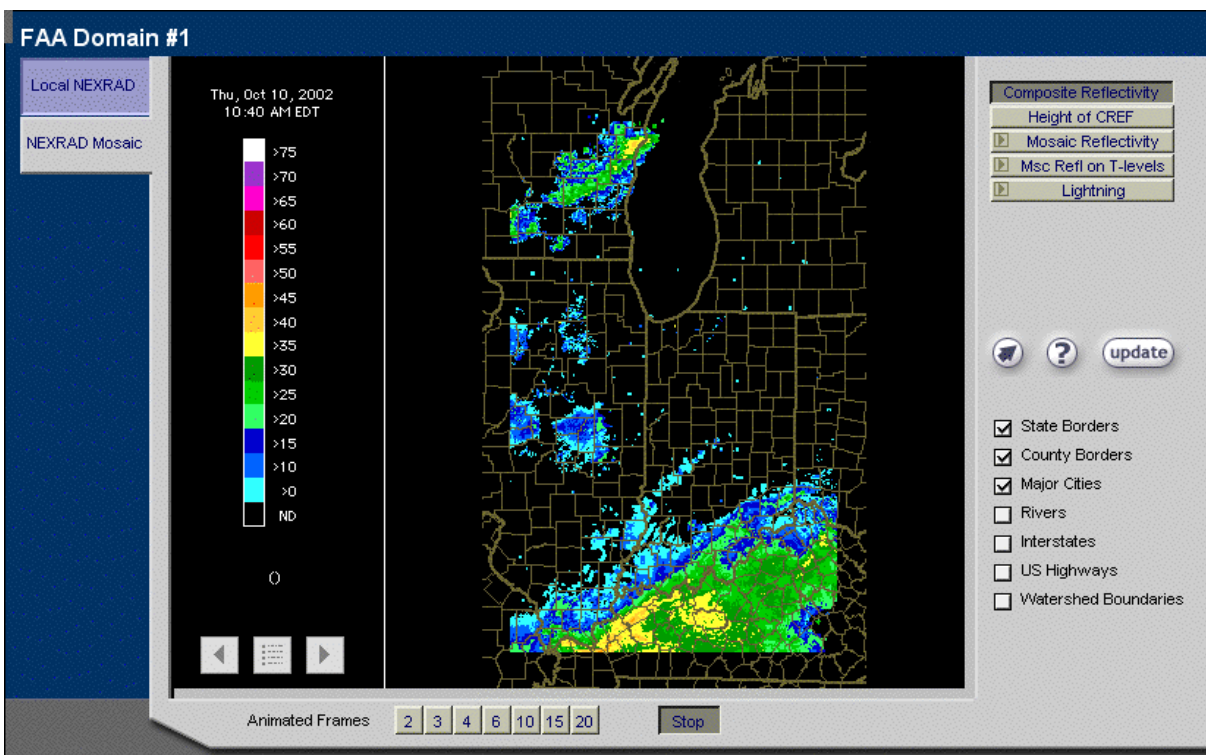


Figure 14.1. Gridded reflectivity over a sub-region of the CIWS domain.

Figure 14.4 is a combined image for the whole FAA northeast corridor. The deliverable 02.6.14.E6 has been completed.

The real-time 3D mosaic data sets are available in NetCDF format. A real-time, anonymous ftp account has been setup for other PDTs (e.g., the NCAR and MIT/LL CWPDT) to pull data for any event.

b) Planned Efforts

The CWPDT has requested the 3D mosaic data sets for several events that occurred in July and August of 2002. Therefore the activities for the next quarter will involve collecting level-2 data and rerun mosaic for archived cases.

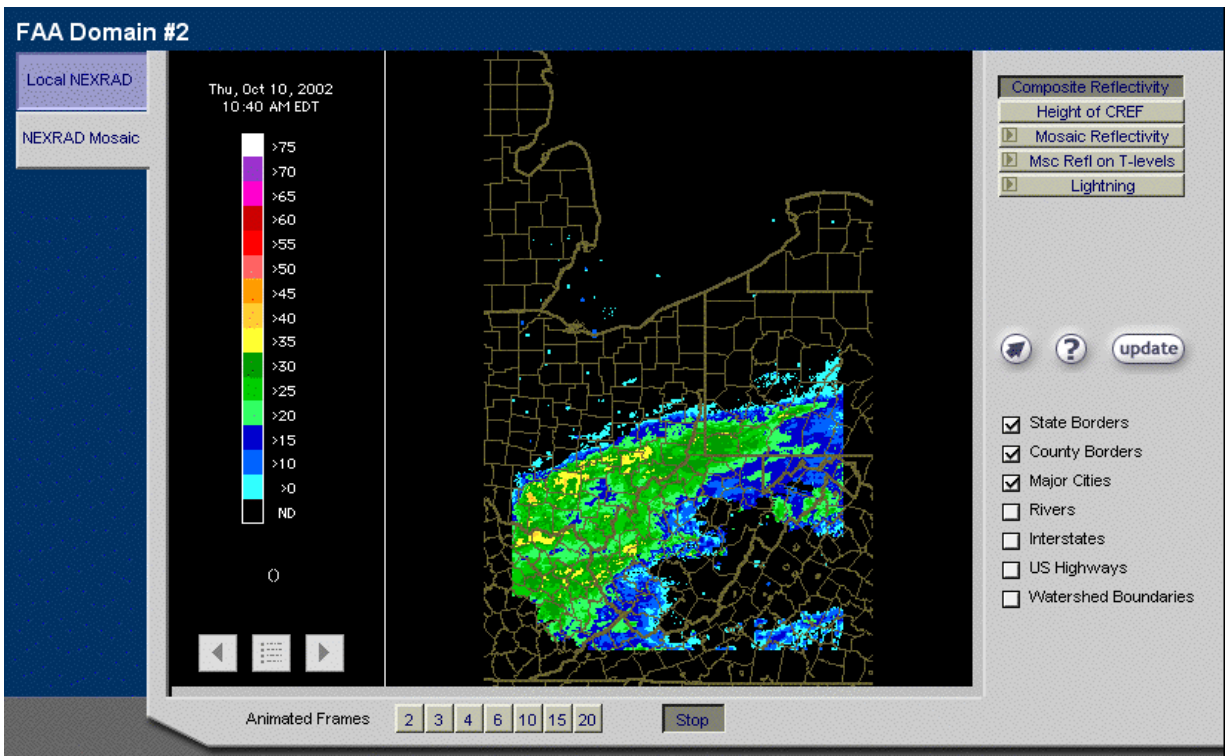


Figure 14.2. Same as 14.1, but for a different sub-region.

c) Problems/Issues

The archived case studies mention above (section b. planned efforts) would require about 350 GB of disk space. Currently the NEPDT 3D mosaic computer has only 100GB space. Thus additional disks may need to be purchased.

d) Interface with other Organizations

NEPDT has been working with CWPDT on 1) accesses to real-time 3D mosaic data in the CIWS domain, and 2) running the 3D mosaic for archived cases.

e) Activity Schedule Changes

None.

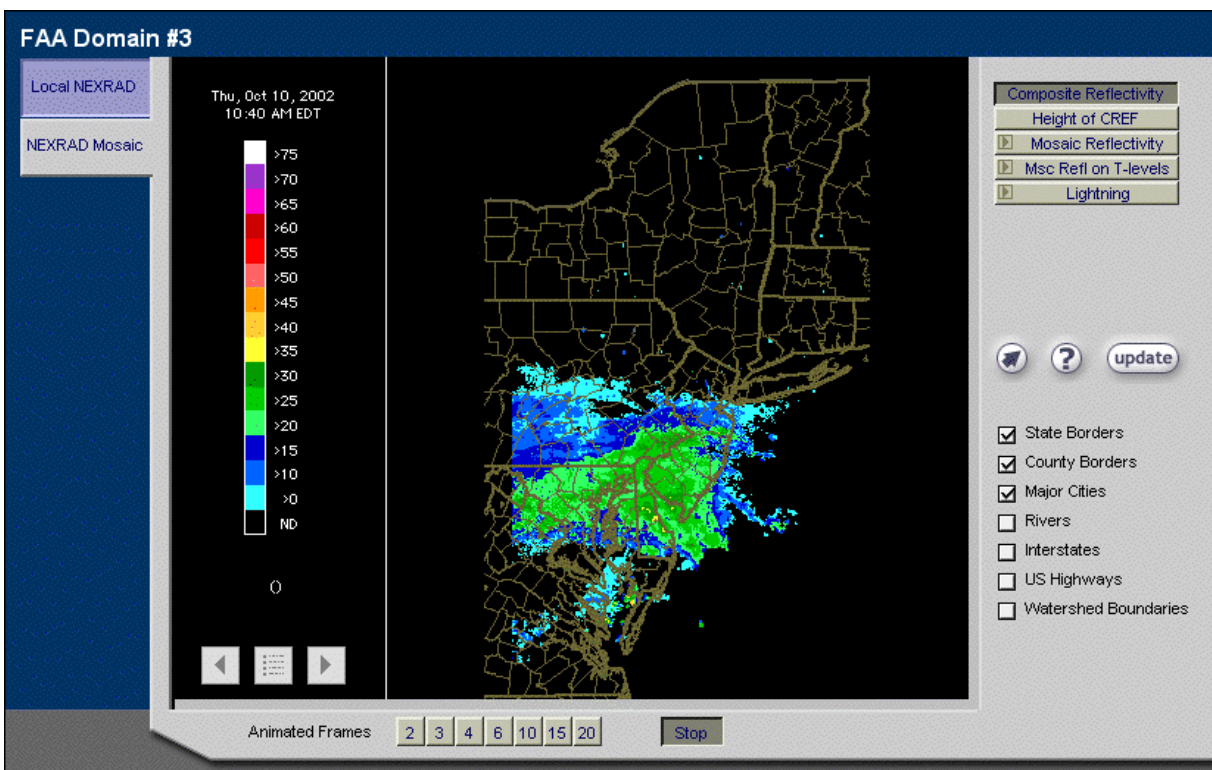


Figure 14.3. Same as 14.1, but for the Eastern-most end of the CIWS domain.

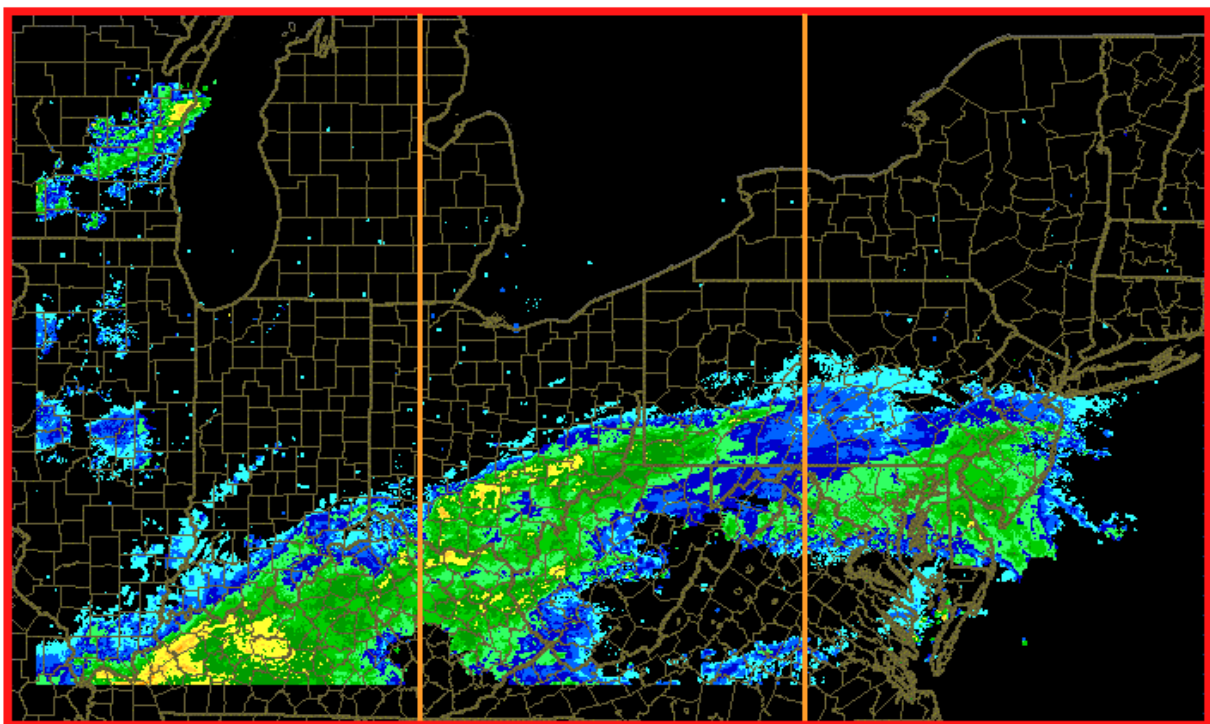


Figure 14.4. Reflectivity over the entire CIWS domain

02.6.15 WARP Activities

Develop strategies and algorithms to remove meteorologically insignificant artifacts; develop next-generation WARP products, based on multi-radar gridded data, suitable for display to air traffic controllers.

b) Planned Efforts

The aim of NSSL's work in support of WARP has recently changed to provide the National Air Traffic Controllers Association (NATCA) with guidance on the accuracy of composite reflectivity products. It has been decided that ORPG product 96 (0-70,000 ft composite reflectivity with AP mitigation) will replace product 36 (0-70,000 ft composite reflectivity without AP mitigation) in the Spring of 2003. NSSL will provide guidance on the accuracy of the AP mitigation scheme used in a variety of meteorological environments. The accuracy of the AP mitigation scheme will be tested in AP events such as nocturnal inversions, convective outflow regions, or events when AP is embedded within convections. But also, the AP mitigation scheme will be examined for cases where no AP is present to determine if it removes precipitation or reduces the magnitude of reflectivity within convective vents. An example when the magnitude of reflectivity associated with isolated convective cells is reduced by the AP mitigation scheme is shown in Fig. 15.1. Approximately 50 nautical miles (nm) south of the radar an east-west line of convective storms is embedded within a region of extensive clutter. After the AP mitigation scheme is used (Fig. 15.2), much of the clutter surrounding the radar is removed, but the magnitude of the convective cells is also significantly reduced from 46-50 dBZ to 18-30 dBZ.

Several test cases have been truthed to separate regions of precipitation and AP and will be used within the examination of AP mitigation accuracy in the composite reflectivity products. Test cases that have been truthed include nocturnal AP, AP coexistent with but not embedded within convection, AP embedded within a mesoscale convective system, and sea clutter. The case shown in Figure 1 will also be used as an example in which the AP mitigation is too aggressive in removing clutter surrounding a radar.

The AP mitigation scheme used within ORPG products 36, 67, and 96. These three products are 0-60,000 ft composite reflectivity images using no AP-mitigation scheme (product 36), an AP-mitigation provided by Lincoln Labs (product, and the same AP-mitigation scheme with a modified set of adaptable parameters.

c) Problems/Issues

None.

d) Interface with other Organizations

None.

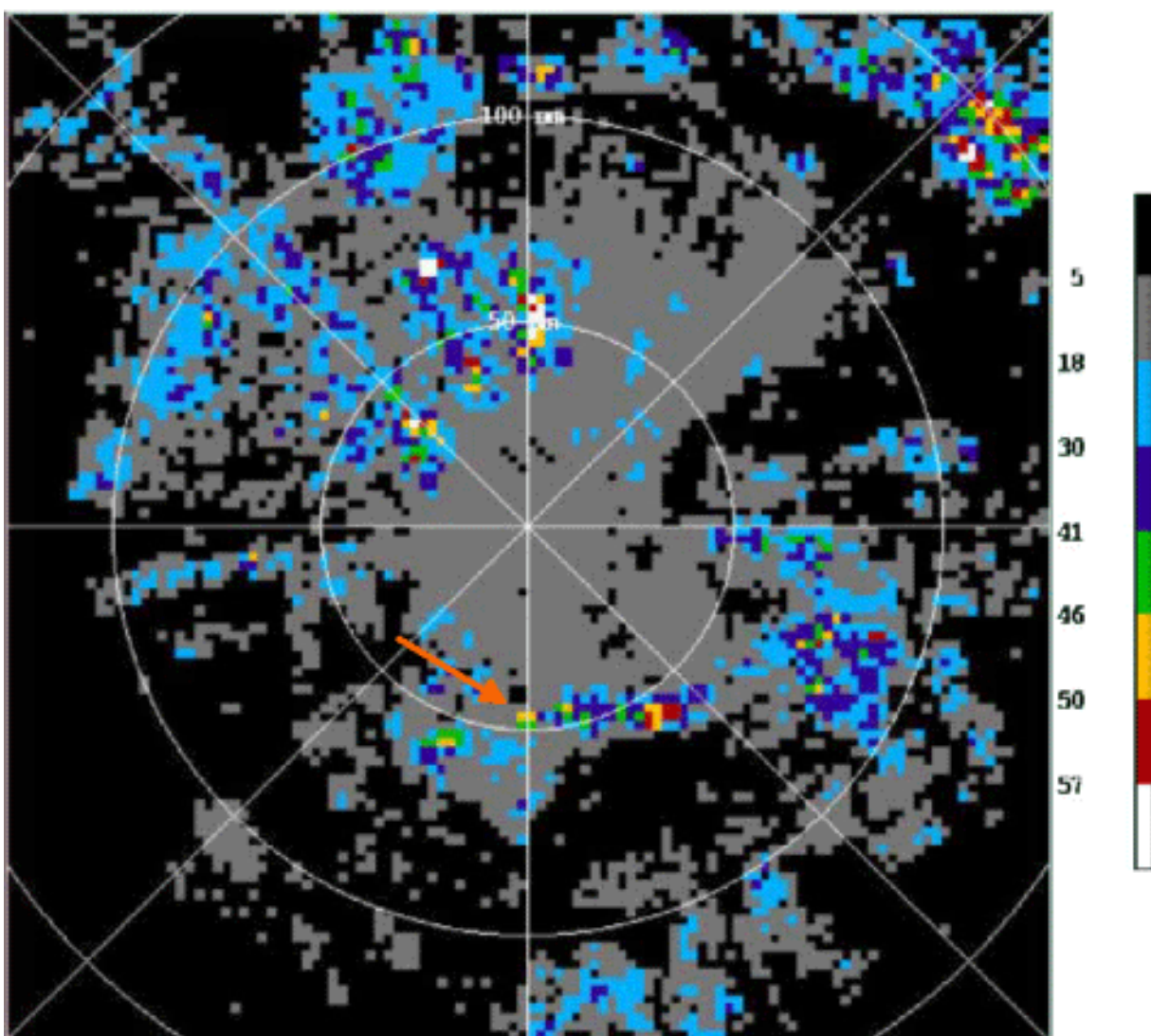


Figure 15.1. Composite Reflectivity without AP mitigation (ORPG product 36) for WSR-88D KFWS on July 13, 1995 at 1338 UTC. Orange arrow denotes line of convective cells. This figure is adapted from figure provided by Tim O'Bannon of the ROC/OSF.

e) Activity Schedule Changes

None.

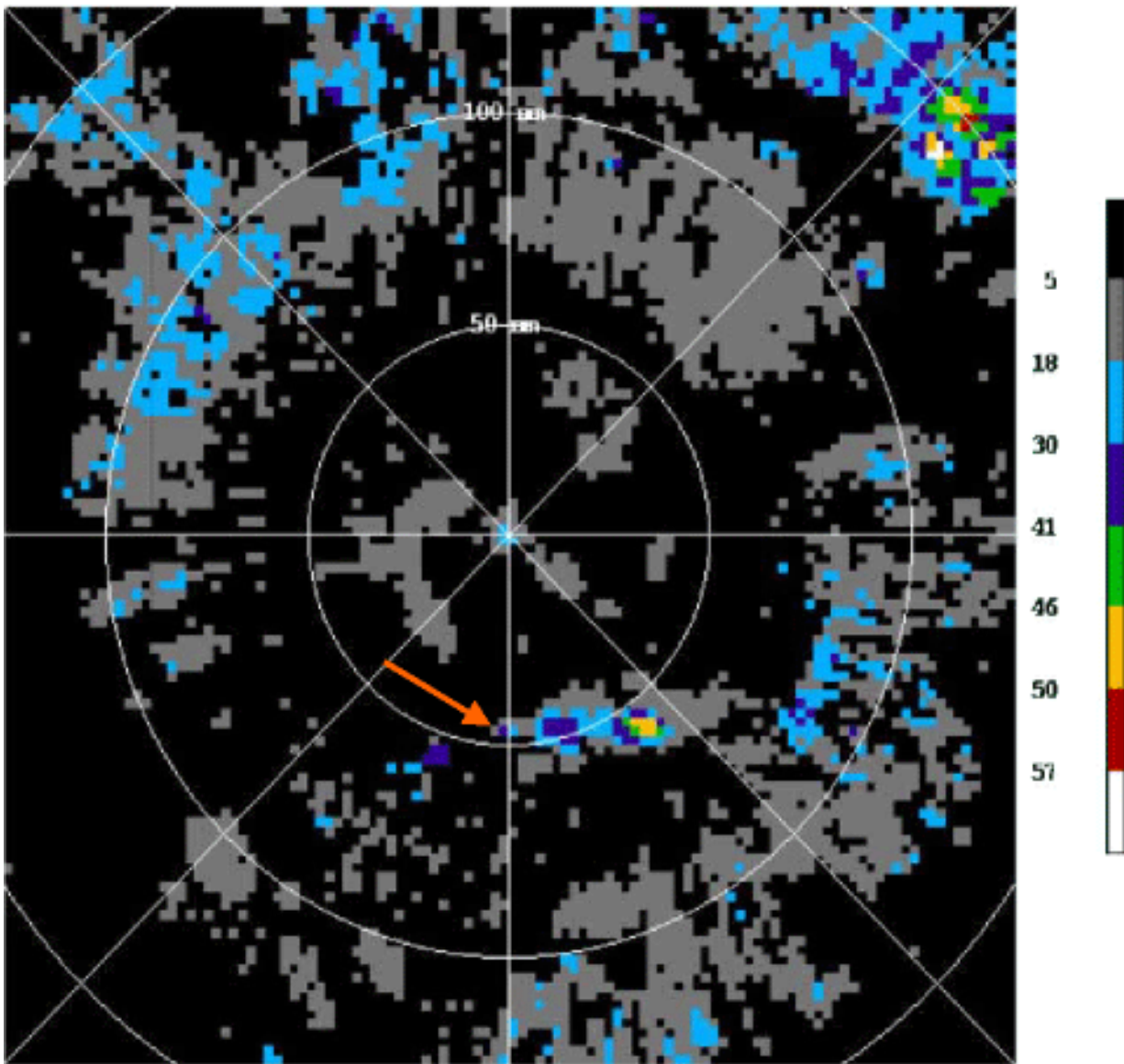


Figure 15.2. Same as Fig. 15.1, except AP mitigation with ORPG product 96 is used on this Composite reflectivity product.

**Freezing Level Detection:
Interim Report**

Report Prepared for the Federal Aviation Administration

30 September 2002

Edward A. Brandes and Kyoko Ikeda

National Center for Atmospheric Research

P.O. Box 3000

Boulder, CO 80307

I. Introduction

Dual-polarization radars typically transmit horizontally and vertically polarized electromagnetic waves and receive backscattered signals. Because illuminated hydrometeors are not spherical and have a distribution of orientations, their backscattering cross-sections are not the same for the two polarizations. Waves propagating through precipitation are subject to scattering, differential attenuation, differential phase shifts, and depolarization. Signal properties change continuously as the waves propagate yielding information regarding particle size, shape, orientation, and thermodynamic phase. Polarimetric measurements are particularly sensitive to the presence of large, wetted particles characteristic of melting layers. The signatures have been exploited to develop an algorithm for detecting the 0°C level in precipitating storms. A capability to retrieve the melting layer has import for the designation of icing hazards, for rain–snow discrimination, and for the Hydrometeor Classification Algorithm.

The purpose of the report is to discuss recent progress toward the development of an algorithm for designating freezing levels. The dataset examined here is mostly from the IMPROVE II field campaign lead by a team of scientists from the University of Washington and conducted during November–December 2002. The goals of the IMPROVE program are to determine the microphysical properties of winter storms in the Pacific Northwest and to improve their representation in mesoscale models. [Information regarding the IMPROVE program can be found at the website <http://improve.atmos.washington.edu>.] Observational platforms for the IMPROVE II field experiment included two research aircraft, the National Center for Atmospheric Research’s S-band polarimetric radar (S-Pol), two Integrated Sounding Systems (ISSs), a mobile sounding system, and local National Weather Service soundings.

Datasets collected during IMPROVE field campaigns provide a good test for algorithm development. Freezing levels are low, and the local terrain is mountainous resulting in extended ground clutter echoes.

II. Overview of the Freezing Level Detection Algorithm

For this study the measurements examined were the radar reflectivity at horizontal polarization (Z_H), the differential reflectivity (Z_{DR}), the linear depolarization ratio (LDR), the co-polar correlation coefficient (ρ_{HV}), and the differential propagation phase (Φ_{DP}). Typical profiles for Z_H , Z_{DR} , LDR, and ρ_{HV} are shown in Fig. 1. The 0°C level, determined from local soundings, is superimposed. Partly melted hydrometeors appear to the radar as raindrops of equivalent size. The reflectivity of melting ice particles increases initially. [Frequently, however, reflectivity begins to increase at temperatures of roughly -5°C as the stickiness of the hydrometeors increases and aggregation occurs. Note the rapid increase in reflectivity that begins well above the melting level.] The reflectivity maximum and its height are dictated by the size of the hydrometeors and the degree of melting. Eventually, reflectivity decreases as melting continues and the particles collapse into raindrops and an increase in terminal velocity removes the particles from the radar volume. In the figure the melting layer signature extends downward to 1.8 km.

Examination of numerous Z_{DR} profiles (e.g., Fig. 1) disclosed a curious spike at the base of the reflectivity bright band (~1 km height) whenever the reflectivity bright band was close to ground. This feature was not present when the melting layer was higher, suggesting that the

pronounced maximum may have resulted from ground clutter contamination. Consequently, Z_{DR} was excluded from the melting layer determinations. Information provided by Z_{DR} is at best redundant; and generally, more precise definition of the melting layer is given by LDR and ρ_{HV} . LDR responds primarily to a distribution of particles whose principal axes are not aligned with the radar polarization. Particle canting causes a small portion of the transmitted energy to “leak” into the orthogonal direction. The leakage is enhanced for large mixed-phase particles. The co-polar correlation coefficient is reduced by a distribution of particle shapes and types and by the presence of large wetted particles.

Freezing level determinations are made by comparing observed vertical profiles of the polarimetric variables to the model profiles in Fig. 2. The goodness of fit is determined for each radar parameter by comparing the observed distribution with the model. The degree of fit is determined by “lagging” the model profile over the observed profile and computing the correlation coefficient. Correlations maximize when the signature extremes line up. Freezing level designations are made by knowing the statistical relationship between the height of signature extremes and the true 0°C level. Based on an inspection of the IMPROVE dataset the offsets were determined to be 0.2 km for radar reflectivity and 0.3 km for the linear depolarization ratio and the correlation coefficient. [These changes represent small climatological adjustments (~0.1 km) from warm season values used previously.] Individual parameter height designations are weighed (after removing profiles with correlation coefficients < 0.7) to find a consensus height. [One half the variance in the observations is explained by the model at this threshold.]

Other algorithm input parameters are

- Elevation of the radar site: 0.475 km
- Radius for horizontal averaging of the radar data: 3 km
- Vertical distance for averaging radar data: 0.2 km
- Depth of the atmosphere where the algorithm is applied: 1 – 4 km AGL.

An attempt was made to use the differential propagation phase measurement for melting layer detection. The notion was that the large particles in the melting layer might behave as Mie scatterers and yield a backscatter differential phase shift that could be used to detect the melting layer. This was not the case however. Weak meteorological signals precluded a significant differential propagation phase shift. Consequently, freezing level detections in this report are made only with the radar reflectivity, linear depolarization ratio, and correlation coefficient parameters.

III. Performance of the freezing level detection algorithm

Figures 3a and 3b show freezing level heights deduced from polarimetric measurements on a 5 km grid array for 1538 UTC and 2018 UTC on 28 November 2002. The designations are based on measurements collected in range-height-indicator (RHI) scans for azimuths between 80 and 141 degrees. The bold value at a grid point is the weighted mean (consensus) height, as estimated from the polarimetric measurements. In most cases the Z_H , LDR, and ρ_{HV} measurements are used. If the correlation coefficient fell below the critical value of 0.7 for a particular parameter, that parameter was deleted. If two parameters fell below the critical value, no estimate was made. The consensus height h_{fzlv} was computed from

$$h_{fzlv} = \frac{\sum_{i=1}^n h_i \cdot r_i^2}{\sum_{i=1}^n r_i^2} \quad [\text{km}]$$

where n is the number of profiles, h_i is the freezing level height for i th parameter, and r_i is the correlation coefficient for the i th parameter. The standard deviation of the estimates was determined from

$$s = \sqrt{\frac{1}{n} \sum_{i=1}^n (h_i - h_{fzlv})^2} \quad . \quad [\text{km}]$$

The standard deviation is the second number given. The remaining number is the number of parameters from which the consensus value and the standard deviation are computed.

It is evident from the two figures that freezing level designations for standard deviations less than 0.1 km are quite stable. Designations are made out to a range of about 30 km. Note that the standard deviation term for the more distant grid points increases. Beyond 30 km designations are hampered by ground clutter and weakening precipitation; freezing level heights became anomalously low for radar reflectivity. [Retrievals for other geographical regions (e.g., Florida) indicate that retrievals can often be made to distances of 50–60 km. At more distant ranges melting layer signatures are essentially suppressed by beam broadening.]

Figure 4 shows a time series of estimated freezing levels using RHI measurements for the period 1440–2200 UTC. Observed freezing level heights from soundings made at the National Weather Service’s office in Salem, OR and from a NCAR mobile sounding unit are also given. Salem is located approximately 60 km north-northwest of the radar, and the mobile launch site was located approximately 55 km to the south-southwest. A “Median” value in Fig. 4 represents the median of freezing level estimates at grid points within 30 km radius of the radar and within the 80–141° sector. The weighted mean (“Wt. Mean” in the figure) is the weighted average of all the possible estimates in the described area. The weights for averaging each polarimetric variable are the correlation coefficients described above. The weights for averaging the consensus estimates are the sum of the correlation coefficients for the individual parameters. Precipitation was uniform and relatively deep across the Oregon Cascades until ~1800 UTC. Consequently, the derived freezing level heights from all estimators show very little scatter. The scatter increased after 1800 UTC as the system became shallow, precipitation weakened, and the freezing level descended. Note that the outliers in the figure are primarily associated with radar reflectivity and recall that they arise from ground clutter problems. Overall, designated freezing levels agree nicely with the rawinsonde observations.

Freezing level designations made with the three polarimetric variables are shown in Fig. 5. Reduced scatter at a particular time suggests that best results are obtained with the linear depolarization ratio.

To determine if regional climatology can influence algorithm performance the relationship between the height of the maximum reflectivity value in the melting layer was compared to the height of the maximum LDR and the minimum ρ_{HV} values in the layer (Fig. 6). Comparisons are shown for several field programs [PRECIP98 (Florida), STEPS (eastern Colorado), CASES (Kansas), TRMM-LBA (Brazil), and MAP (Italy)]. The data were collected by pointing the radar antenna vertically with the exception of the IMPROVE experiments where they are computed from RHIs at a range of 10 km. Inspection reveals that heights determined from LDR and ρ_{HV} for warm season events in Kansas and Brazil are depressed from those

derived from reflectivity by approximately 0.2 km. In contrast, the offset for the winter IMPROVE datasets is about 0.1 km. This supports the earlier discussion suggesting that some tuning of the Freezing Level Detection Algorithm is in order for local climatology.

It was suspected that the depressions in Fig. 6 were related to precipitation intensity. This was confirmed by plotting the depression of the LDR melting layer maximum and the ρ_{HV} minimum from the bright band reflectivity maximum against the magnitude of the reflectivity maximum (Fig. 7). For weak precipitation the height of melting layer extremes are roughly the same. As the precipitation intensity increases, LDR and ρ_{HV} signatures lower in height with respect to reflectivity. The increased depression most likely is due to the presence of larger hydrometeors. Accounting for hydrometeor size through the reflectivity parameter could be a refinement to the method.

IV. Conclusions and future activities

Further testing of the Freezing Level Detection Algorithm confirmed its utility in winter precipitation in the Oregon Cascades and for retrieving the 0°C level when it is close to ground. Application revealed a small dependence on the local precipitation climatology. In addition, sensitivity to precipitation intensity (and perhaps characteristics of the frozen hydrometeors) was detected. Such issues represent relatively minor adjustments. Unfortunately, precise comparisons between aircraft-determined and radar-determined 0°C levels necessary for such improvements were not possible for the datasets examined here. Nevertheless, comparisons with nearby atmospheric soundings suggest that freezing level designations with the algorithm should be within ± 0.1 km. This should be sufficient for many applications.

The Freezing Level Detection Algorithm has been installed on NCAR's S-Pol radar and will run in real time during future field operations. Plans call for incorporating the retrievals into NCAR's Hydrometeor Classification Algorithm. Submission of a formal paper on the retrieval method is also planned.

S-Pol

Date: 112801

Time: 163147 UTC

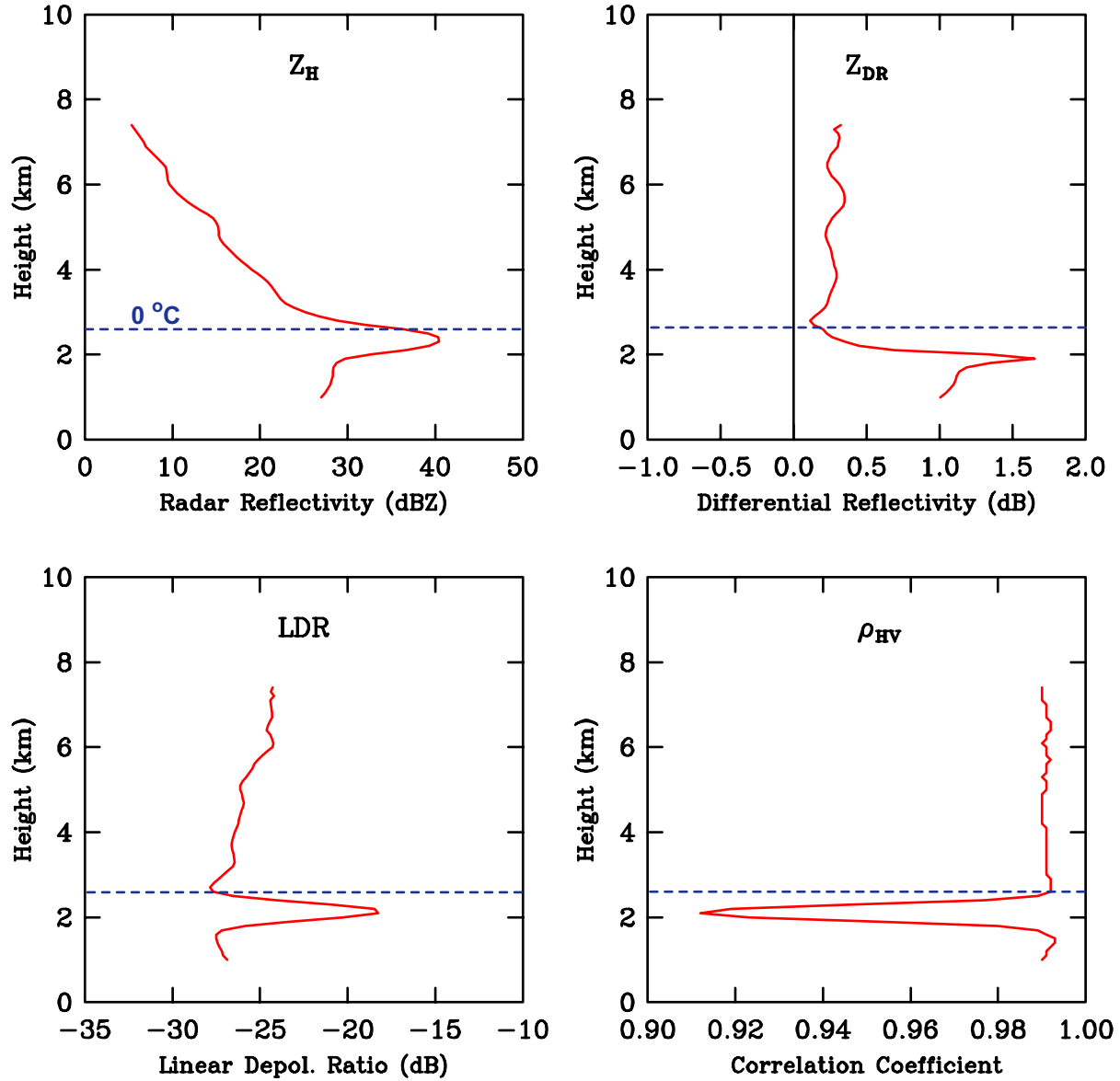


Figure 1: Profiles of polarimetric radar measurements [radar reflectivity (Z_H), differential reflectivity (Z_{DR}), linear depolarization ratio (LDR), and co-polar correlation coefficient (ρ_{HV})] obtained during IMPROVE II (28 November 2001, 163147 UTC). The estimated 0°C level, based on the average of two soundings, is shown. Heights are kilometers above mean sea level.

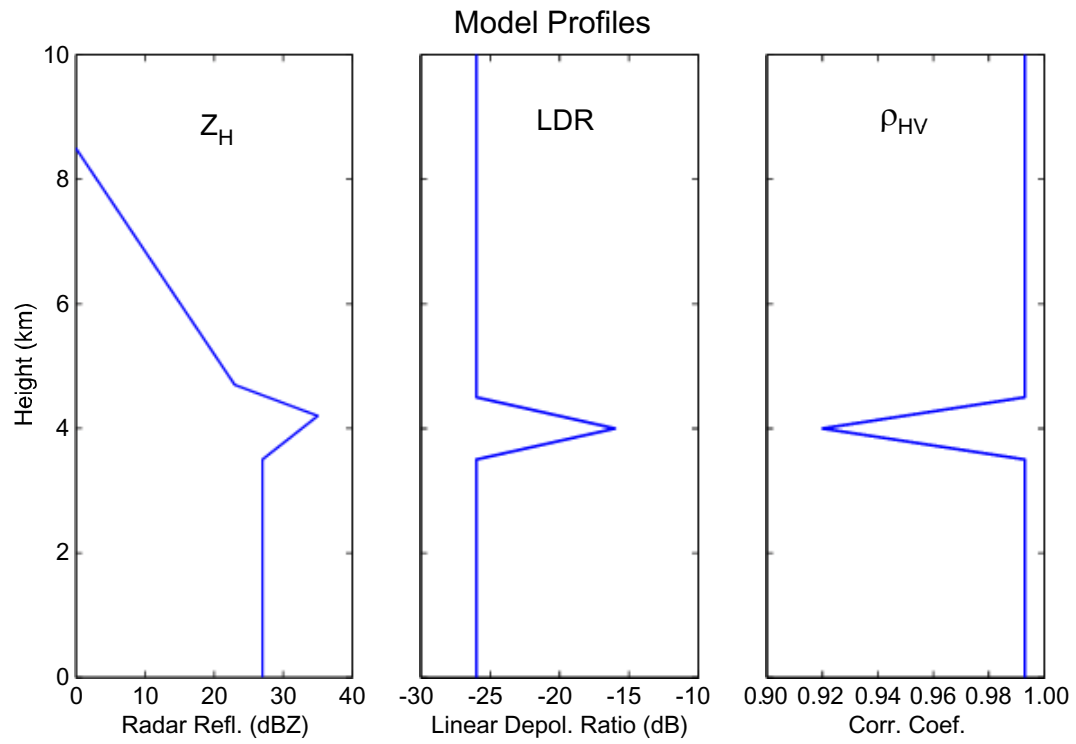


Figure 2: Model polarimetric profiles for reflectivity, linear depolarization ratio, and correlation coefficient.

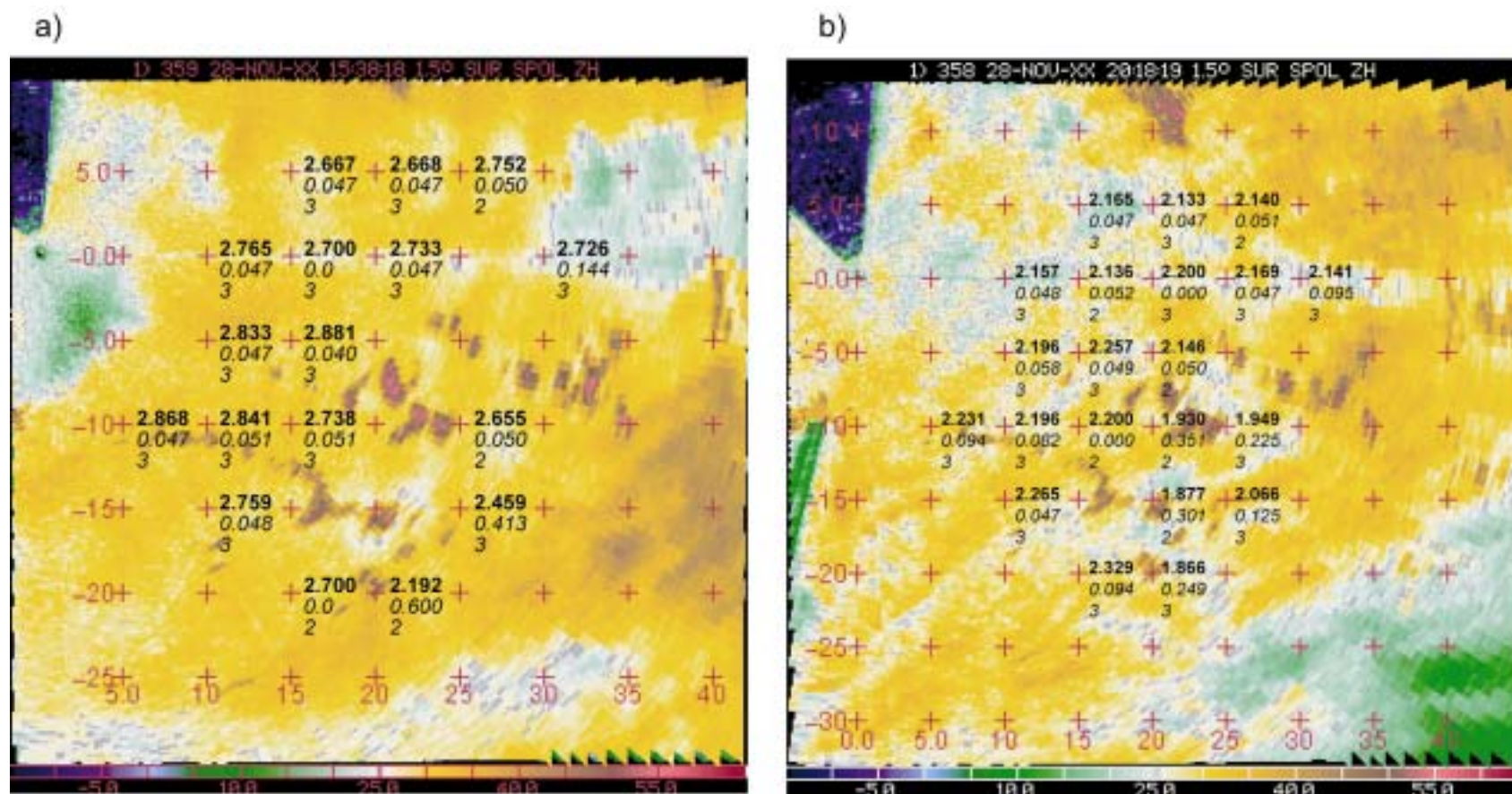


Figure 3: Retrieved heights of the melting layer (0°C surface) at (a) 1538 and (b) 2018 UTC on 28 November 2001. The grid spacing is 5 km. The upper number is the consensus freezing level height (km, MSL), the middle number is the standard deviation of the estimated heights, and the lower number is the number of parameters having a correlation with the model of >0.7 .

IMPROVE II : Freezing Level Height 28 November 2001

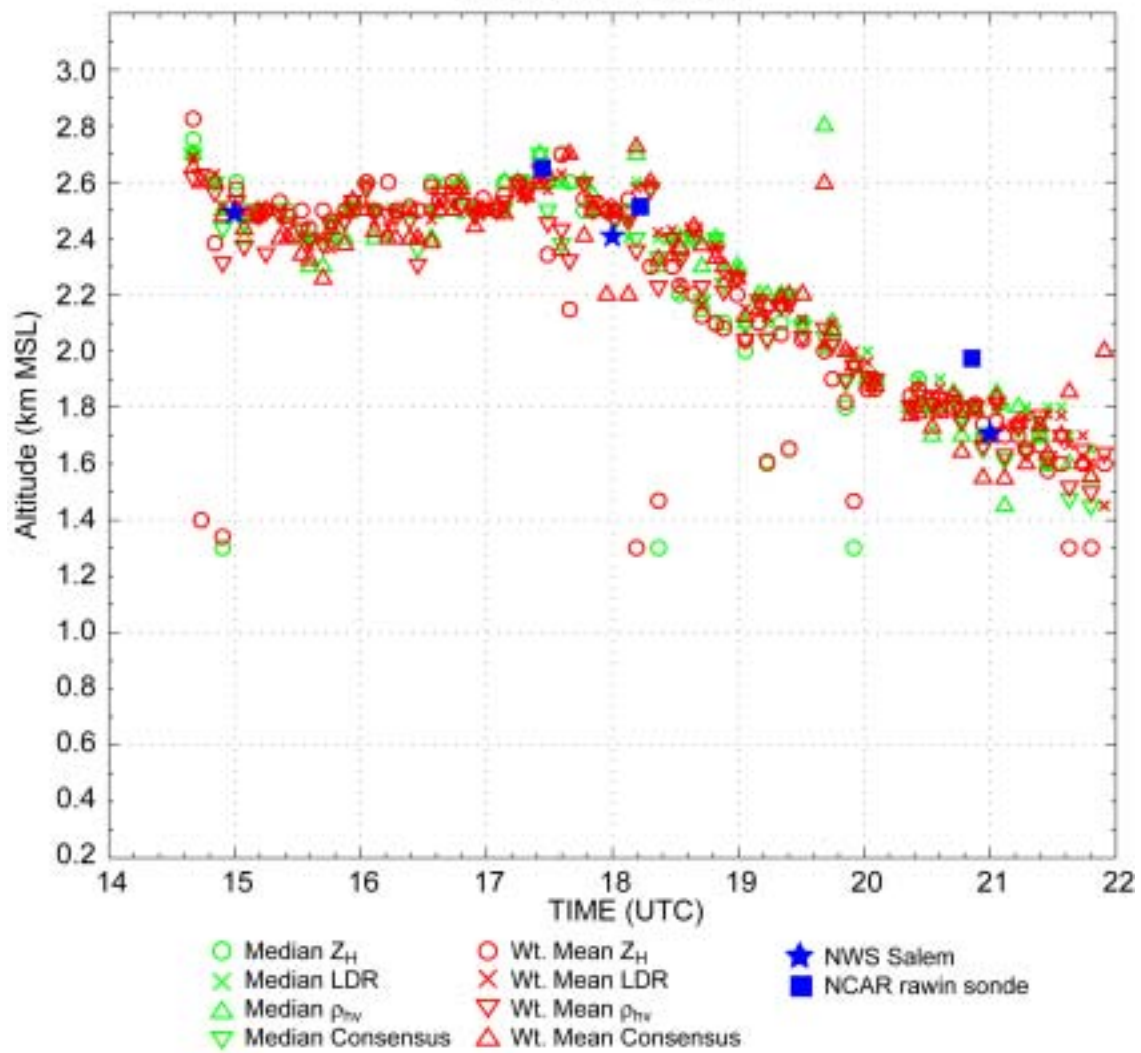


Figure 4: Time series of consensus freezing level heights for 28 November 2001 (1400–2200 UTC). “Median” and “Weighted” values are shown (see text).

IMPROVE II : 28 November 2001
Estimated Freezing Levels

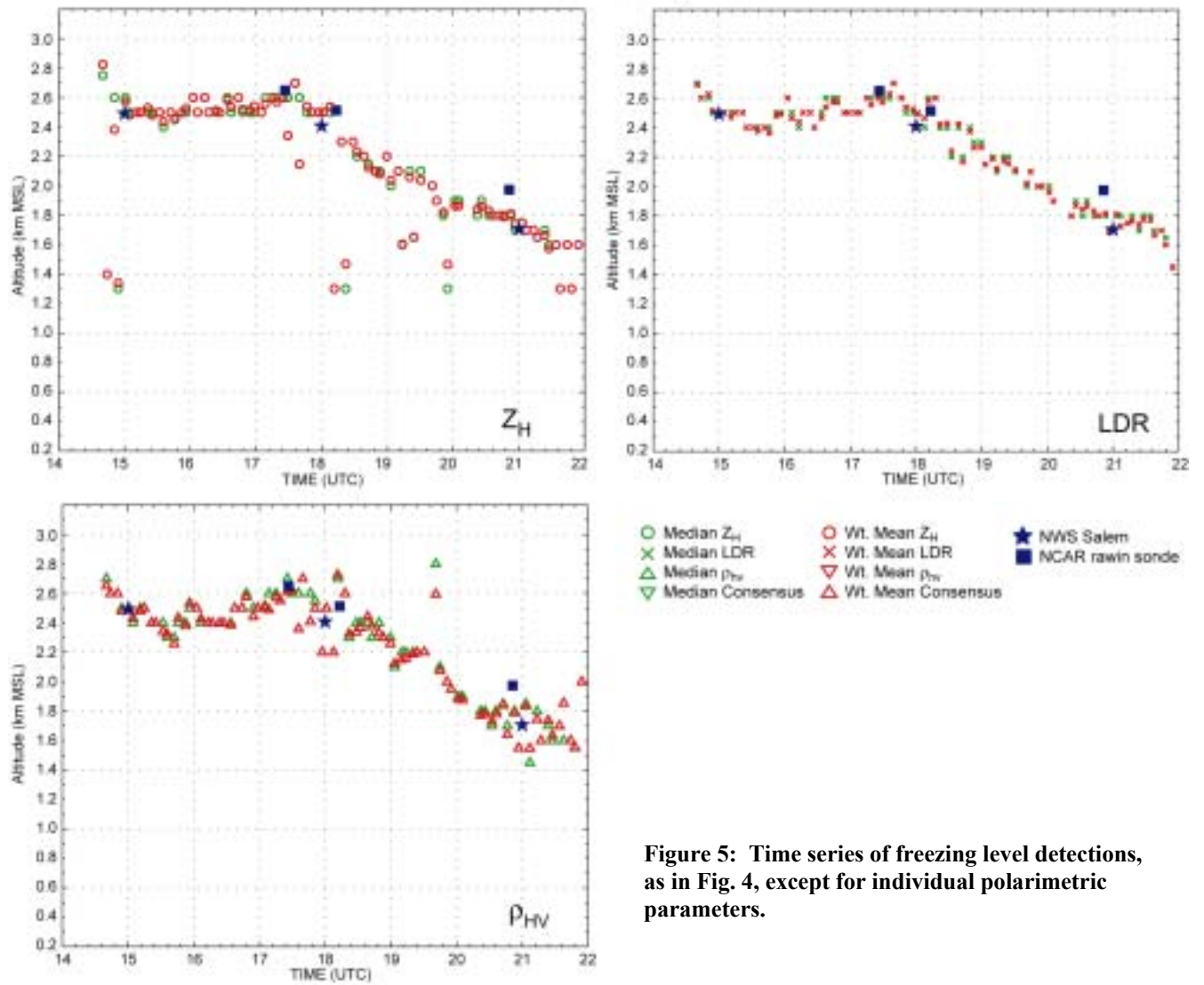


Figure 5: Time series of freezing level detections, as in Fig. 4, except for individual polarimetric parameters.

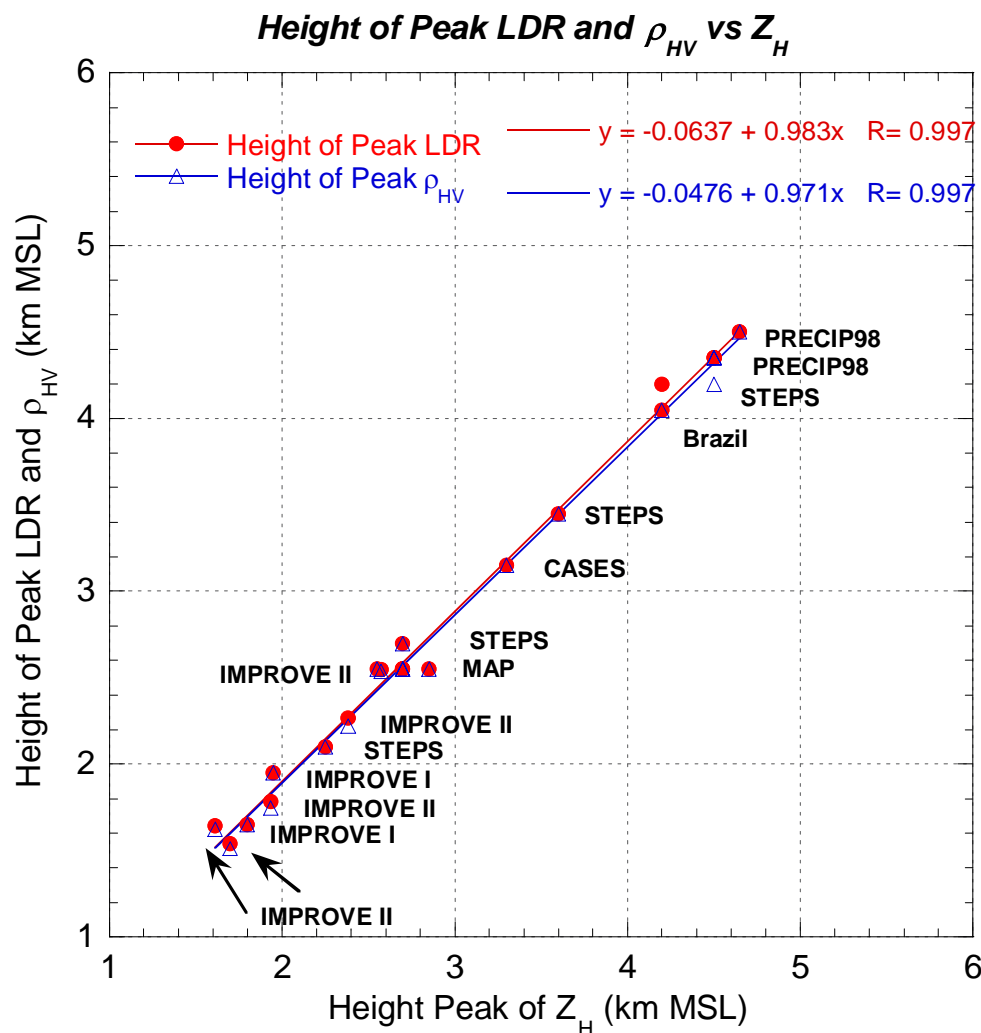


Figure 6: Height of melting layer peak LDR and minimum ρ_{HV} plotted against the height of the reflectivity maximum for selected examples from several field programs.

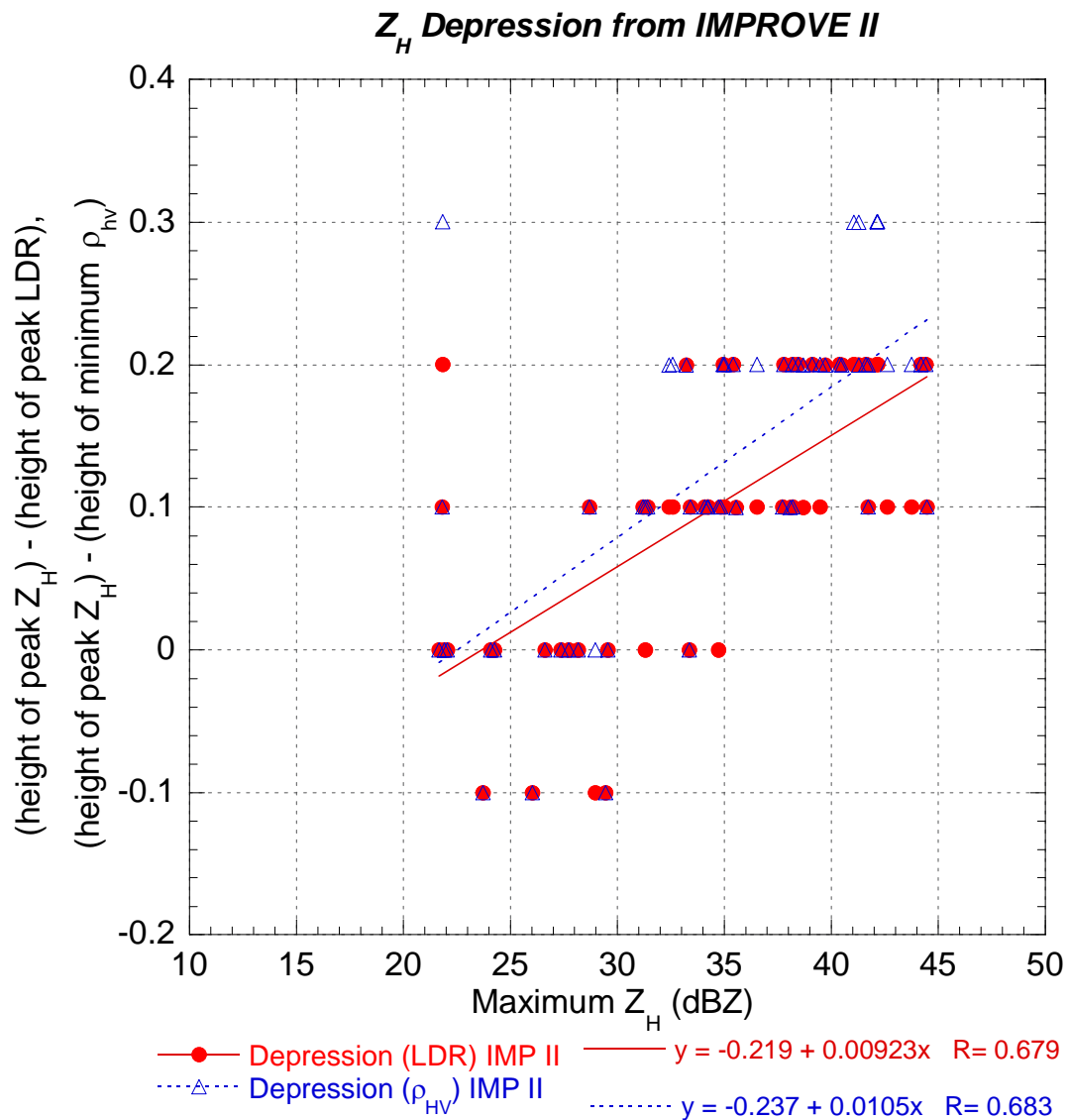


Figure 7: Depression of melting layer peak LDR and minimum ρ_{HV} from reflectivity maximum plotted versus the magnitude of the reflectivity maximum.

Hydrometeor Classification Algorithm Development: Progress Report

Report Prepared for the Federal Aviation Administration

30 September 2002

Edward A. Brandes and Kyoko Ikeda

National Center for Atmospheric Research
P.O. Box 3000
Boulder, CO 80307

1. Introduction

Because polarimetric radar measurements are sensitive to particle size, shape, orientation, phase (liquid or solid), and density (wet, dry, aggregates, or rimed), particular hydrometeor types have characteristic signatures.¹ The ensemble of measurements [principally radar reflectivity (Z_H), differential reflectivity (Z_{DR}), linear depolarization ratio (LDR), co-polar correlation coefficient (ρ_{HV}), and differential propagation phase (Φ_{DP})] can be used to ascertain the dominant hydrometeor types within a radar measurement volume (Vivekanandan et al. 1999). Classifications are based on knowledge gained from numerous observational studies and simulations [see Table 8.1 of Doviak and Zrnić (1993)]. Because polarimetric signatures for specific hydrometeors typically overlap, designations are usually based on a “fuzzy logic” approach.

The purpose of this report is to give an overview of recent activities regarding this ongoing research task. Topics covered are the verification of frozen hydrometeor classifications, the investigation of icing events, and the retrieval of raindrop size distributions from polarimetric measurements. Activities regarding rain-snow discrimination were discussed in a paper presented earlier this year at the 10th Conference on Aviation Range, and Aerospace Meteorology (Brandes et al. 2002). A related activity, described in a separate report, is the development of an algorithm to automatically designate the freezing (0°C) level in the atmosphere. Knowing the freezing level height is crucial for hydrometeor classification. Other accomplishments this past year were the purchase of two particle cameras to document frozen hydrometeor types in winter storms and the acquisition of a video disdrometer with opportunity funds from NCAR’s director.

2. Evaluation of Frozen Particle Designations

NCAR’s polarimetric Hydrometeor Classification Algorithm (HCA) currently makes designations in 17 categories. There is much activity to determine which categories are justifiable, to improve detections, and to verify algorithm designations. Examples of ice particle designations and in situ particle observations from the IMPROVE II field program are presented in Figs. 1 and 2. [Analysis of this dataset, collected during November and December 2001, has just begun.] The upper four panels in each figure show hydrometeor images obtained with a Particle Measuring Systems, Inc. two-dimensional (2D-C) cloud probe. Figure 1 depicts dendrites and aggregates observed at approximately 2153 UTC on 28 November 2001. [Note that the particles are poorly sampled by the 2D-C probe. Images from IMPROVE II instruments designed to detect precipitation-sized hydrometeors are not yet available.] The aircraft operated at an altitude of 4.65 km above mean sea level; the temperature was –11°C. The lower right panel shows a histogram of particle designations made with the classification algorithm along the aircraft’s flight path. The designations are for radar measurement volumes within 1 km horizontal and 0.5 km vertical distances of the aircraft track, a 10 s segment ~1 km in length. Classifications are primarily for dry snow (DSNW), defined as moderate-size unwetted and

¹ For a detailed description of the polarimetric variables and their properties readers are refer to Doviak and Zrnić (1993). A tutorial on polarimetric variables and potential algorithms can be found on the website <http://www.osf.noaa.gov/app/> (Annual Algorithm R&D Summary: 2000 Report).

unrimed aggregates with low density. Membership values (at 0.5 weight) for this classification are

Z_H	12.5 to 32.5 dBZ
Z_{DR}	-0.5 to 1.25 dB
LDR	-27 to -22 dB
ρ_{HV}	0.975 to 1.00
K_{DP}	-0.025 to $0.15^\circ \text{ km}^{-1}$ at 12.5 dBZ
K_{DP}	-0.025 to $0.19^\circ \text{ km}^{-1}$ at 32.5 dBZ

where K_{DP} , the specific differential phase, is the range derivative of Φ_{DP} .

A secondary classification in Fig. 1 is for irregular ice crystals (IRIC). This designation is intended to represent oriented particles that are tumbling, oddly shaped crystals, and small aggregates. The classification assumes the following membership values

Z_H	-9 to 25 dBZ
Z_{DR}	-0.05 to 0.85 dB
LDR	-27 to -22 dB
ρ_{HV}	0.975 to 1.00
K_{DP}	-0.05 to $0.15^\circ \text{ km}^{-1}$

It is clear that there is considerable signature overlap for dry snow and irregular ice crystals. Final classification, as either dry snow or irregular ice crystals, is based on a weighting of all parameters, but reflectivity is the primary distinguishing factor for these two particle types. The philosophy is that low reflectivity (e.g., 0 dBZ) would not be representative of snow and that a moderate reflectivity of 30 dBZ would be too great for ice crystals. The relative transition between these two precipitation types is by necessity “fuzzy”.

Figure 2 shows particle images from 1818 UTC on 29 November 2001. This event was characterized by weak stratiform precipitation with weak embedded convection (Fig. 3). Observed hydrometeors on 29 November are more spherical and rounded than those in Fig. 1, an indication that the particles are rimed. However, designations are predominantly for dry snow and irregular ice crystals. Reflectivity values in the region averaged ~ 15 dBZ. This is somewhat higher than suggested by the particles shown in Fig. 2. Hence, larger particles must have been present. [Designations for drizzle and light rain are discussed in the next section.] The representativeness of the aircraft observations and radar measurements is just one of the difficulties in verifying the HCA. Radar measurement volumes are on the order of 1 km^3 , and the measurements are sensitive to the largest particles present. Sampling volumes with aircraft-based sensors are many orders of magnitude smaller than that of the radar and essentially representative of hydrometeors along a line drawn through a particular storm. The largest particles are rarely detected by aircraft.

3. Detection of potential icing conditions

Storm penetrating aircraft that provide the datasets for our studies frequently experience icing conditions. The lower left hand panel in Fig. 1 shows that light icing was occurring at the time the hydrometeor images were obtained. The image on the lower right shows two particles that are believed to be droplets with diameters of 0.15–0.2 mm. [Digitization of the images causes a non-circular shape.] Although the reflectivity of these particles is enhanced by their being liquid, the radar reflectivity measurements respond primarily to the larger frozen particles. Hence, the designation for the radar volumes is for dry snow and irregular ice crystals. The drizzle and light rain designations in Fig. 2 (at an altitude of 2.11 km and a temperature of -8°C) are examples of potential icing conditions that are sometimes identified with the HCA. Also, a number of supercooled liquid designations on the edges of the convective cell and in fringe areas of the stratiform precipitation shield can be seen among the hydrometeor classifications in Fig. 3. [See Ellis et al. 1999,2001 for additional examples.] These measurement volumes are characterized by radar returns suggestive of liquid precipitation. The utility of the liquid hydrometeor designations for specifying potential icing hazards is being examined. Because the number of events for which icing occurred and quality polarimetric radar data are available is limited, we will attempt to increase the data sample with observations from a radiometer, which measures the total liquid content along the radar beam, as a surrogate for aircraft observations.

4. Retrieval of particle distributions

During the past year significant progress has been made with other funding in the retrieval of raindrop size distributions and related parameters from polarimetric radar data. The technique, described by Zhang et al. (2001), assumes that drops are represented by a gamma size distribution and makes use of the reflectivity and differential reflectivity measurements and an empirical relation derived from disdrometer observations. The technique has been verified with disdrometer measurements and by comparison with other proposed drop-size distribution (DSD) retrieval techniques.

Figure 4 shows the low-level wind field in a thunderstorm complex observed on 22 September during PRECIP98. Heavy contours are radar reflectivity, light solid contours show regions with updrafts $> 1 \text{ m s}^{-1}$, light dashed contours are downdrafts $> 1 \text{ m s}^{-1}$, and the storm-relative horizontal wind field is shown by vectors. Retrieved DSD parameters (the logarithm of the total drop concentration, drop median volume diameter, liquid water content, and rain rate) are presented in Fig. 5. Median volume diameters can be used to identify and quantify large drop events. Rain rates derived from polarimetric measurements have proven to be more accurate than those derived from radar reflectivity. The improvement is particularly significant at the higher rain rates where visibility and runway braking conditions may be impaired. An advantage with the Zhang et al. retrieval technique is that prior knowledge of the DSD, necessary for deriving power-law rainfall estimators, is not needed.

A capability to monitor DSDs has import for understanding precipitation processes, particularly when coupled with hydrometeor classifications, and for verification of quantitative precipitation forecasts. Future efforts will attempt to extend the methodology to winter precipitation. The added complication is the density of the hydrometeors.

5. Future plans

Plans call for continued verification of the Hydrometeor Classification Algorithm with emphasis on frozen hydrometeors and winter precipitation. This effort, which currently involves the use of radar measurements and in situ aircraft observations, will be extended with microphysical observations to be collected this coming winter with polarimetric radar, particle cameras, and a video disdrometer. The data will also be used in exploratory studies seeking to improve the quantification of winter precipitation.

The evaluation of polarimetric radar measurements for designating potential icing conditions will continue with the IMPROVE datasets. To mitigate verification issues related to differences between radar and aircraft sampling times and measurement locations, radiometer observations will also be examined.

Efforts to verify the HCA to date have taken advantage of related field programs involving polarimetric radars. These programs have their own objectives. Measurements made and in situ observations obtained are often not adequate for verification purposes. The proposed Joint Polarization Experiment (JPOLE) will be the first field program to specifically address the verification issue. Other field programs such as the Alliance Icing Research Study II (AIRS II) also offer unique opportunities to examine the utility of polarimetric radar measurements in other climatological regimes and for winter precipitation. Hence, plans call for participation in the planning and conducting of these important field programs.

REFERENCES

- Brandes, E. A., J. Vivekanandan, and R. Rasmussen, 2002: Rain–snow discrimination with polarimetric radar. *Preprints, 10th Conf. on Aviation, Range, and Aerospace Meteor.*, Portland, Oregon, Amer. Meteor. Soc., 108-111.
- Ellis, S. M., J. Vivekanandan, E. A. Brandes, 1999: Verification of polarimetric radar based cloud microphysical results using aircraft observations. *Preprints, 29th International Conf. on Radar Meteor.*, Montreal, Quebec, Canada, Amer. Meteor. Soc., 180-183.
- Ellis, S. M., J. Vivekanandan, S. Göke, E. A. Brandes, J. Stith, R. J. Keeler, 2001: In-situ verification of remote aircraft detection using S-band polarization radar measurements. *Preprints, 30th Conf. on Radar Meteor.*, Munich, Germany, Amer. Meteor. Soc., 168-170.
- Doviak, R. J., and D. S. Zrnić, 1993: *Doppler Radar and Weather Observations*, Academic Press, 562 pp.
- Vivekanandan, J., D. S. Zrnić, S. M. Ellis, R. Oye, A. V. Ryzhkov, and J. Straka, 1999: Cloud microphysics retrieval using S-band dual-polarization measurements. *Bull. Amer. Meteor. Soc.*, **80**, 381-388.
- Zhang, G., J. Vivekanandan, and E. Brandes, 2001: A method for estimating rain rate and drop size distribution from polarimetric radar measurements. *IEEE Trans. Geosci. Remote Sensing*, **39**, 830-841.

IMPROVE II : 28 November 2001, 21:52:43 UTC
Altitude 4.65 km MSL

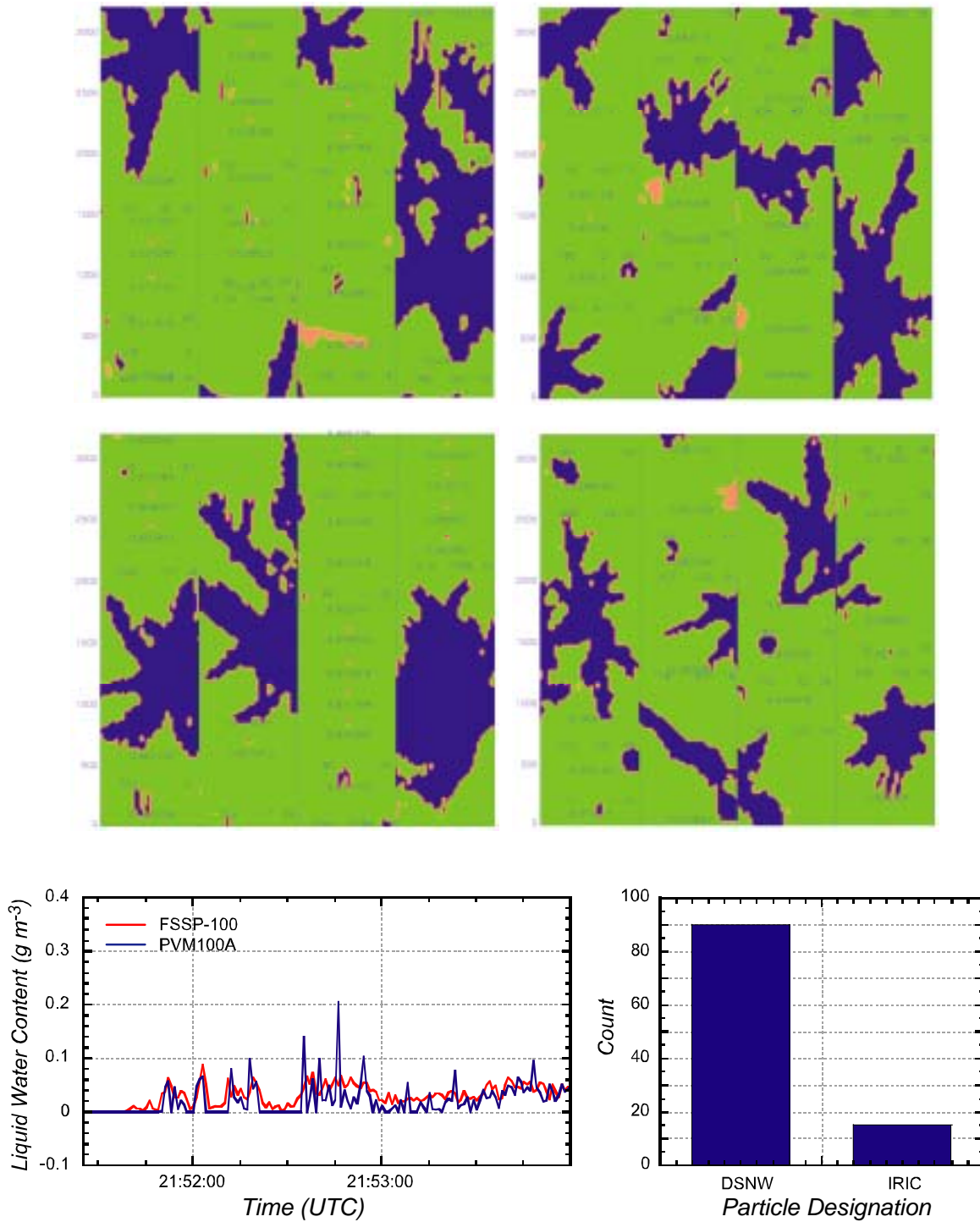


Figure 1: Hydrometeor images (upper 4 panels) obtained by aircraft at ~2153 UTC on 28 November 2001, radar-derived particle designations (lower right panel), and aircraft measured icing (lower left panel). The aircraft altitude was 4.65 km (MSL) and the temperature was -11°C . DSNW and IRIC indicate dry snow and irregular ice crystals, respectively.

IMPROVE II : 29 November 2001, 18:18:15 UTC
Altitude 2.11 km MSL

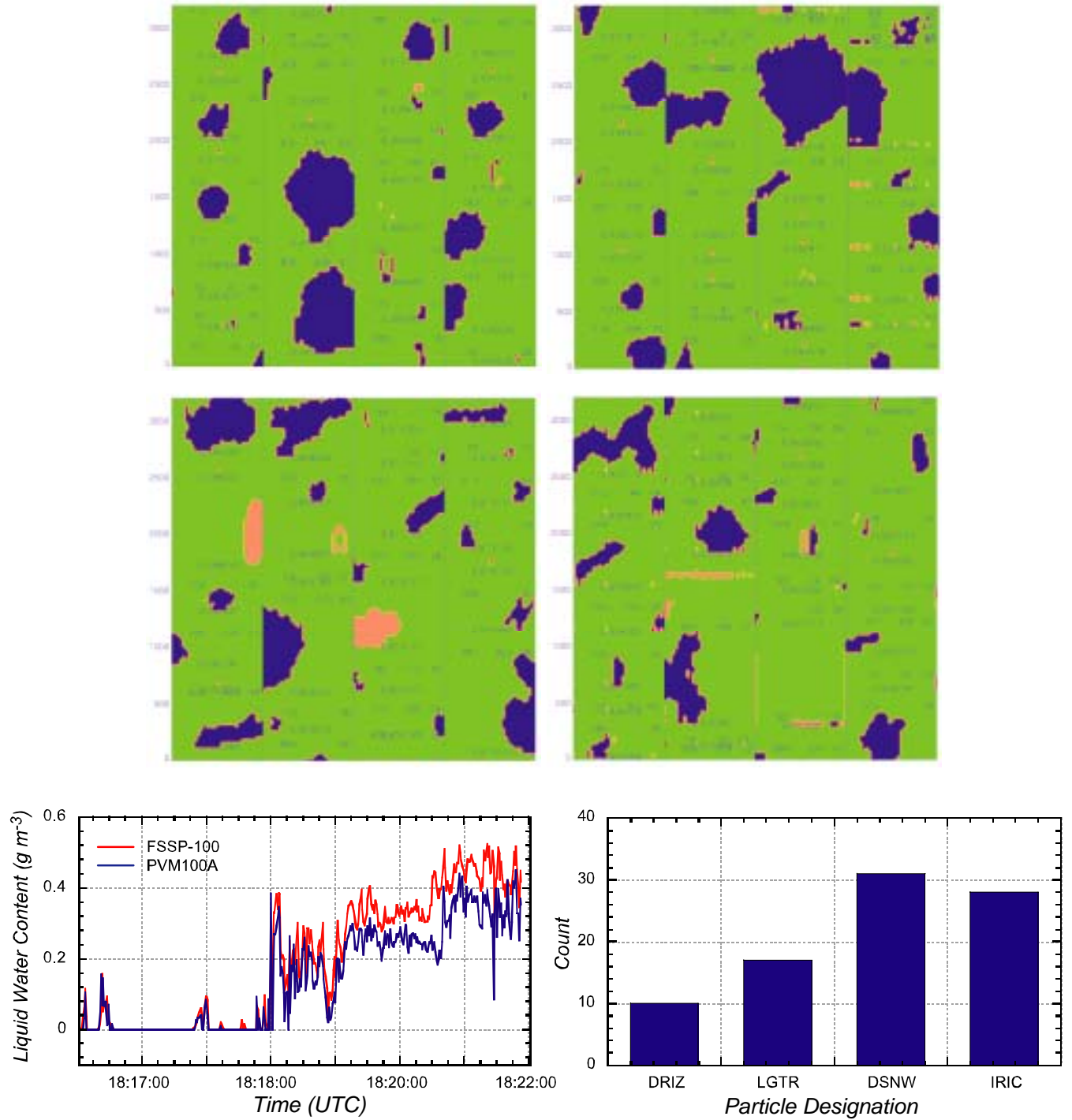


Figure 2: As in Fig. 1, except for 1818 UTC on 29 November 2001. The aircraft altitude was 2.11 km (MSL) and the temperature was -8°C . DRIZ and LGTR indicate drizzle and light rain.

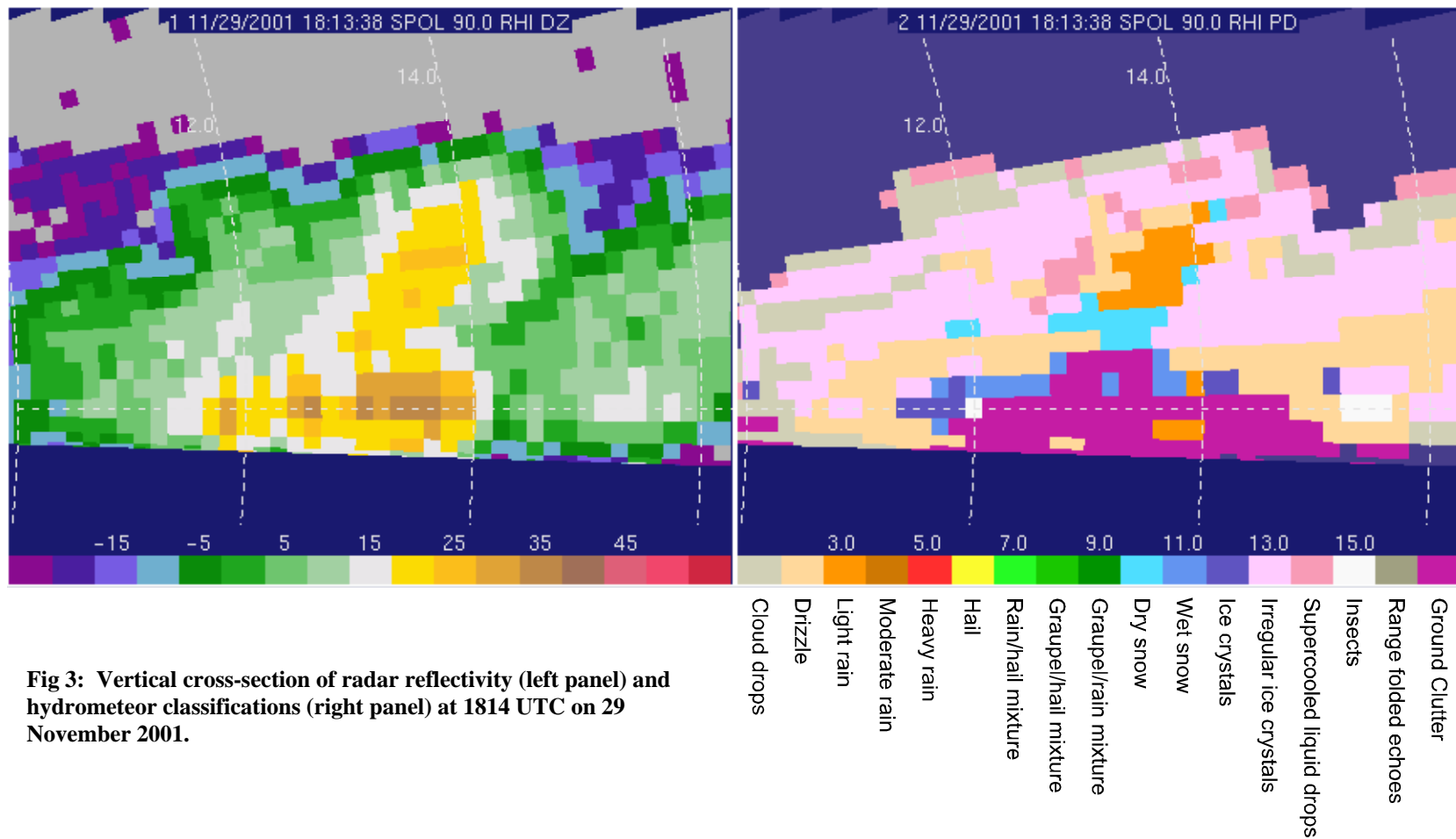


Fig 3: Vertical cross-section of radar reflectivity (left panel) and hydrometeor classifications (right panel) at 1814 UTC on 29 November 2001.

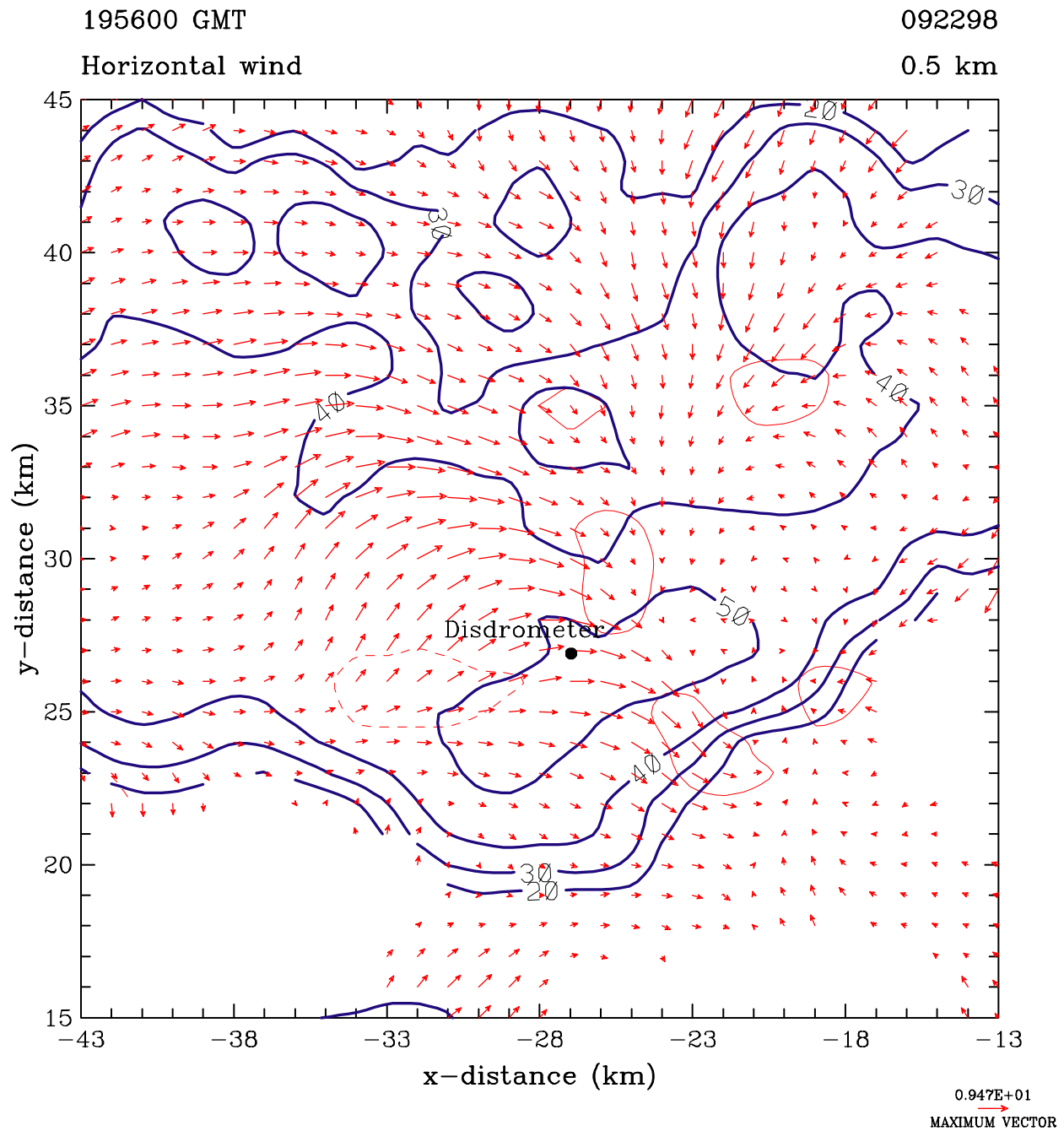


Figure 4: Dual-Doppler wind analysis of a thunderstorm complex observed on 22 September 1998. Storm-relative horizontal winds are shown by vectors. Heavy contours are radar reflectivity from the KMLB WSR-88D, light solid contours are updrafts $> 1 \text{ m s}^{-1}$, and light dashed contours are downdrafts $> 1 \text{ m s}^{-1}$. The analysis is for 0.5 km AGL.

DSD Parameter Retrieval
22 September 1998, 1956 UTC

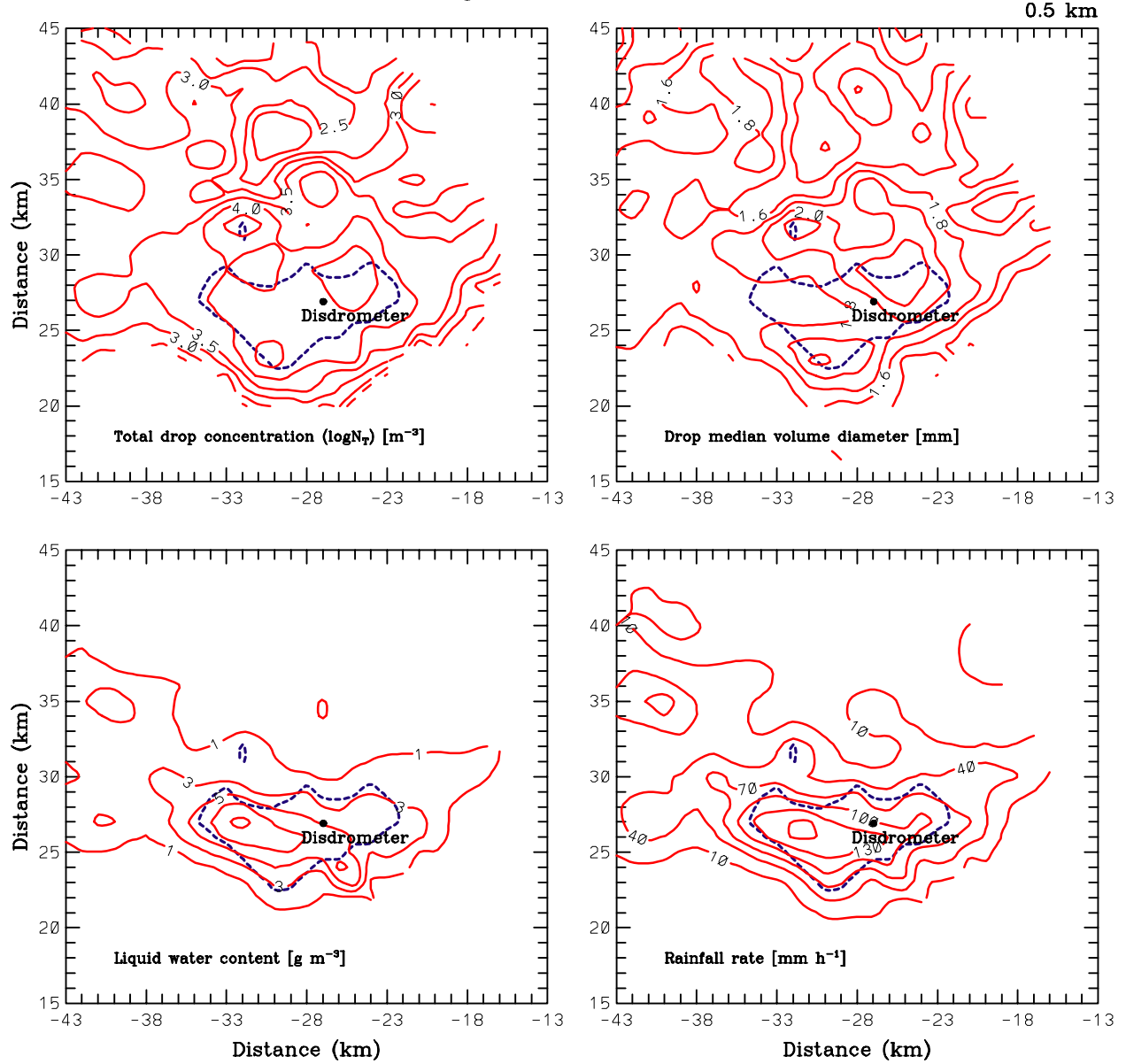


Figure 5: Radar-retrieved DSD parameters (logarithm of the total drop concentration, drop median volume diameter, liquid water content, and rain rate) for the dataset in Fig. 4. The 50 dBZ radar reflectivity contour from NCAR's S-Pol radar is overlaid (heavy dashed).

Status of NEXRAD Enhancements PDT Deliverables September 30 2002

Legend: ■ Task proceeding on schedule; ☑ Task complete; ☐ Task incomplete and overdue.

NEPDT Deliverable and Related Task	Lead Org	Due	Stat	Comment
02.6.2.1 (Polarization) HCA Development	NSSL	31/03/02	☑	Start 01/10/01
02.6.2.2 (Polarization) Data Continuity	NSSL	31/03/02	☑	Start 01/10/01
02.6.2.3 (Polarization) Confidence Factors	NSSL	31/03/02	☑	Postponed
02.6.2.4 (Polarization) JPOLE Workshop	NSSL	15/06/02	☑	Start 15/05/02
02.6.2.5 (Polarization) WSR-88D(P) Data Quality Evaluation	NSSL	30/09/02	☑	Start 01/10/01
02.6.2.6 (Polarization) Real-Time HCA Test	NSSL	30/09/02	☑	Start 01/10/01
02.6.2.7 (Polarization) JPOLE Phase I Data Collection, Warm Rain	NSSL	30/09/02	☑	Start 01/04/02
02.6.2.8 (Polarization) JPOLE Phase I Data Collection: Plan Cold-Season	NSSL	30/09/02	☑	Start 01/07/02
02.6.2.9 (Polarization) WSR-88D Cloud Tops, Thickness	NSSL	31/04/02	☑	Start 01/10/01
02.6.2.10 (Polarization) Signal Processing to Decrease VCP Time	NSSL	30/09/02	☑	Start 01/10/01
02.6.2.11 (Polarization) Freezing Level	NCAR	30/09/02	☑	Start 01/10/01
02.6.2.12 (Polarization) Non-Precip HCA verification	NSSL	30/09/02	☑	Start 01/05/02
02.6.2.13 (Polarization) Cloud Water	NCAR	30/09/02	☑	Start 01/10/01
02.6.2.14 (Polarization) Hardware Calibration Technique	NSSL	30/09/02	☑	Start 01/10/01
02.6.2.15 (Polarization) Sea Clutter Mitigation	NSSL	30/09/02	☑	Start 01/10/01
02.6.3.1 (Circulation Algorithm) MDA/TDA Performance during CIWS	NSSL	30/09/02	☑	Start 01/08/02
02.6.4.1 (Technical Facilitation) Polarization Display Development	NSSL	30/09/02	☑	Start 30/10/01
02.6.4.2 (Technical Facilitation) WDSS-II Multi-Radar Display Development	NSSL	30/09/02	☑	Start 01/10/01
02.6.4.3 (Technical Facilitation) WDSS-II Multi-Sensor Display Development	NSSL	30/09/02	☑	Start 01/10/01

02.6.4.4 (Technical Facilitation) Spectrum-Level Data QC	NCAR	30/09/02	<input checked="" type="checkbox"/>	Start 01/10/01
02.6.9.1 (Composite Products) BBID using WSR-88D and TDWR	NSSL	30/06/02	<input checked="" type="checkbox"/>	Start 01/03/02
02.6.9.2 (Composite Products) BBID Testing in CIWS Region	NSSL	30/09/02	<input checked="" type="checkbox"/>	Start 01/07/02
02.6.11.1 (Volume Coverage Patterns) Data Collection	NSSL	30/09/02	<input checked="" type="checkbox"/>	Start 01/10/01
02.6.12.1 (Product Implementation) Collaboration, Product Development	NSSL	Quarterly	<input checked="" type="checkbox"/>	Start 01/10/01
02.6.14.1 (Multi-Radar Composites) CPU Requirements	NSSL	31/03/02*	<input checked="" type="checkbox"/>	Start 01/02/02
02.6.14.2 (Multi-Radar Composites) Mosaic Strategies	NSSL	30/06/02	<input checked="" type="checkbox"/>	Start 01/01/02
02.6.14.3 (Multi-Radar Composites) Real-Time Testing	NSSL	30/09/02	<input checked="" type="checkbox"/>	Start 01/07/02
02.6.14.4 (Multi-Radar Composites) Define Analysis Domain and Grid Resolution	NSSL	31/01/02*	<input checked="" type="checkbox"/>	Start 01/10/01
02.6.14.5 (Multi-Radar Composites) Real-Time CIWS Support	NSSL	31/03/02*	<input checked="" type="checkbox"/>	Start 12/31/01
02.6.14.6 (Multi-Radar Composites) Display Systems	NSSL	30/09/02	<input checked="" type="checkbox"/>	Start 01/07/02
02.6.15.1 (WARP support)Adaptable Parameter Development	NSSL	30/06/02	<input checked="" type="checkbox"/>	Start 01/10/01
02.6.15.2 (WARP Support) Next Generation Algorithms	NSSL	30/09/02	<input checked="" type="checkbox"/>	Start 01/04/02

* Due date revised thru AWRP POC.